



Comparative verification of discrete and smeared numerical approaches for the simulation of hydraulic fracturing

Keita Yoshioka¹ · Francesco Parisio¹ · Dmitri Naumov¹ · Renchao Lu^{1,2} · Olaf Kolditz^{1,2} · Thomas Nagel^{1,3} 

Received: 30 March 2018 / Accepted: 21 January 2019
© Springer-Verlag GmbH Germany, part of Springer Nature 2019

Abstract

The numerical treatment of propagating fractures as embedded discontinuities is a challenging task for which an analyst has to select a suitable numerical method from a range of options. Since their inception in the mid-80s, smeared approaches for fracture simulation such as non-local damage, gradient damage or more lately phase-field modelling have steadily gained popularity. One of the appeals of a smeared implicit fracture representation, the ability to handle complex topologies with unknown crack paths in relatively coarse meshes as well as multiple-crack interaction and multiphysics, is a fundamental requirement for the numerical simulation of hydraulic fracturing in complex situations which is technically more difficult to achieve with many other methods. However, in hydraulic fracturing simulations, not only the prediction of the fracture path but also the computation of fracture width and propagation pressure (frac pressure) is crucial for reliable and meaningful applications of the simulation tool; how to determine some of these quantities in smeared representations is not immediately obvious. In this study, two of the most popular smeared approaches of recent, namely non-local damage and phase-field models, and an approach in which the solution space is locally enriched to capture a strong discontinuity combined with a cohesive-zone model are verified against fundamental hydraulic fracture propagation problems in the toughness-dominated regime. The individual theoretical foundations of each approach are discussed and differences in the treatment of physical and numerical properties of the methods when applied to the same physical problems are highlighted through examples.

Keywords Phase field method · Non-local damage · Cohesive zone models · Brittle fracture · Hydraulic fracturing · OpenGeoSys · GeomInt · GEMex

✉ Thomas Nagel
thomas.nagel@ifgt.tu-freiberg.de

Extended author information available on the last page of the article

Mathematics Subject Classification 74: Mechanics of deformable solids · 35: Partial differential equations · 65: Numerical analysis

1 Introduction

Simulations of hydraulically driven fracture propagation is still a challenging task in computational mechanics that involves moving boundaries, fluid–structure interaction, strongly discontinuous fields and can in certain cases also entail complex rheological behaviour of the fluids and solid constituents. Which specific approach is most suited to represent the combined problem of pressurization and propagation is still under debate. This contribution aims specifically at comparing two distinct families of numerical approaches: continua with embedded discontinuities (cohesive-zone models) and smeared approaches (phase-field and non-local damage).

The scientific interest in hydraulic fracturing has increased rapidly in the recent past driven by a diverse range of technological applications including productivity enhancements in unconventional fossil fuel reservoirs (Economides and Nolte 2000), the stimulation or enhancement of geothermal reservoirs (Legarth et al. 2005), the assessment of barrier integrity in subsurface energy or waste storage applications (Minkley et al. 2016; Johnson et al. 2004), the safe operation of mines and boreholes (Jiang et al. 2016; Morita et al. 1990), but also the stability of fluid-filled biomaterials undergoing rapid loading (Böger et al. 2017). During the injection of fluid into a fracture, the coupling between hydraulic and mechanical processes spans a wide range of regimes where one or several of the following processes interact: toughness-controlled fracture propagation, dissipative processes in the solid material itself, viscous dissipation within the injected fluid, leak-off into the surrounding porous medium, fluid lag and suction at the crack tip upon fracture propagation, etc. Which of these processes is relevant or even dominant in a particular application depends on material properties, boundary conditions, and the process itself (Detournay 2016). For a low viscosity of the injected fluid and for a very low permeable rock matrix with high toughness, the hypothesis of a toughness-dominated propagation regime can be applied. In this work, we have considered water at room temperature as the injected fluid in a ultra low-permeable and high-toughness metamorphic rock (gneiss) so that the hypothesis of a toughness-dominated regime applies.

Numerical methods are a great asset in unravelling the complex physical mechanisms and in designing controllable stimulation protocols. As previously mentioned, the numerical treatment of crack propagation in general, and with fluid–structure interaction in particular, presents the analyst with a host of numerical challenges that are primarily associated with the creation of new boundary surfaces. The location and time of their creation as well as their topology are generally not known a priori and hence an outcome of the solution process itself. These boundaries can be conceptualised in a number of ways: they can be explicitly modelled by, e.g., remeshing (Bouchard et al. 2000; Meyer et al. 2004; Branco et al. 2015), which presents the additional problem of having to assign boundary conditions to the new surfaces including potential contact formulations and leaves the question of how to model processes that might occur within the newly created fracture space, such as fluid flow. A second approach makes use of

the fact that fracture surfaces coincide in the reference configuration and can hence be conceptualized as strong discontinuities in the displacement field. Standard finite element methods have C^0 -continuity requirements on primary variables. As such, the ansatz and test function spaces need to be enriched by functions which can capture the displacement jump across the crack tip. Additional enrichments can make use of asymptotic solutions known from fracture mechanical theories to improve numerical performance and decrease mesh sensitivity. An example is crack-tip enrichment by the Westergaard displacement fields (Budyn et al. 2004). These ideas have led to the development of eXtended and Generalized Finite Element Methods (XFEM, GFEM) (Moës et al. 1999; Belytschko et al. 2001, 2009; Gasser and Holzapfel 2005; Fries and Belytschko 2006; Khoei et al. 2012). In their general formulation, the implementational overhead is significant compared to a standard FEM in particular when propagation problems with arbitrary crack topologies are considered in three dimensions where merging and branching are allowed (Belytschko et al. 2001, 2003; Duarte et al. 2007). An extension to multi-physical problems is of course possible (Khoei 2014; Meschke and Leonhart 2015), although it adds additional complexities as the nature of the discontinuity in the various fields relevant for heat transport, multi-phase flow etc. is not always straight-forwardly understood (Zhang et al. 2013; Gordeliy and Peirce 2013; Chessa and Belytschko 2003). In a hydro-mechanical setting, Watanabe et al. (2012) developed a scheme where the local enrichment is introduced by lower-dimensional interface elements (LIE) located at the element boundaries of the full-dimensional domain mesh. Aside from this topological limitation, most advantages of an XFEM scheme are retained while drastically reducing the implementational effort, e.g. by avoiding the need for element splitting and integration routines.

To ease the modelling of the failure process itself and supported by observations in many materials that local failure happens somewhat gradually and covers a fracture process zone, cohesive zone models based on so-called traction-separation laws (TSLs) have been developed (Needleman 1990a,b). They have been successfully applied in the fracture of concrete, composite materials and many others (Nguyen et al. 2001; Elices et al. 2002).

To alleviate some of the difficulties related to these models such as spurious stress transfers, mesh-orientation dependencies, crack merging and branching, discontinuities in multi-physical fields and to be able to utilize standard C^0 -continuous FEM software, smeared approaches to fracture have been introduced in which the fracture is not conceptualized as a sharp interface but as a smooth transition zone spanning a characteristic length scale. This transition zone of decreased to null stress transfer can be seen as a purely mathematical concept to regularise a discontinuity but can also be considered to have physical significance in the context of distributed micro-damage coalescing to a macroscopic fracture as well as of fracture process or dissipation zones (Brace et al. 1966; Bažant 1991; Diederichs 2003; Hoek and Martin 2014). Among these methods, gradient-damage (Peerlings et al. 1996; Pham et al. 2011; Alessi et al. 2015; Nedjar 2016) and phase-field methods (Bourdin et al. 2000; Miehe et al. 2010; Kuhn and Müller 2010; Borden et al. 2012; Wheeler et al. 2014; Ambati et al. 2015) are among the most prominent. They are sometimes referred to as weakly non-local, where strongly non-local models (Bazant and Jirasek 2002; He et al. 2015; Silani et al. 2016; Vtorushin 2016) are a third category of smeared models in which the material

response at a given point is influenced by long-range interactions with neighbouring points falling into a given radius. These approaches offer the additional benefit of linking the classically separate theories strength of materials and fracture mechanics (Klinsmann et al. 2015; Tanné et al. 2018) and can be interpreted based on common physical origins such that they can be transferred into each other (Kuhl et al. 2000; de Borst and Verhoosel 2016a).

Aside from their numerical advantages and disadvantages, motivating the development of hybrid schemes (Giovanardi et al. 2017), it is imperative that all approaches be able to quantify certain key system properties and their evolution to be able to capture the physics of hydraulic fracturing appropriately. Such quantities include the stress fields and intensities, energy release rates, crack advancement in both direction and increment, etc. Of particular relevance in hydraulic fracturing is also the computation of the fracture opening as it determines the hydraulic properties of the fault and the resulting energy dissipation in the fluid and due to fluid–solid interaction. Discrete approaches are ideally suited for quantifying fracture opening and for including fracture-specific constitutive laws for flow and deformation, but present difficulties when dealing with complex topologies including the propagation/merging/branching of cracks in three-dimensional settings (Roth et al. 2016; Fries et al. 2014; Meschke and Leonhart 2015). In smeared approaches, while adept at handling such complex topologies, it seems less straight-forward to quantify fracture volume, aperture, permeability, and even crack length (Klinsmann et al. 2015). These questions need to be addressed in order to allow the analyst to freely select the most suitable method for a given problem.

In this paper we compare three distinct numerical methods, one discrete and two smeared ones, in their ability to capture hydraulically induced fracture propagation in a toughness-dominated regime and to quantify key variables such as fracture opening displacement, fracture volume, fracture length, and critical propagation pressures. The three methods are: (1) the lower-dimensional interface elements (LIE) with local enrichment developed by Watanabe et al. (2012) and extended here by a cohesive-zone approach based on a bi-linear TSL; (2) a linear-elastic phase-field model for brittle fracture; (3) a non-local elasto-plastic damage model for brittle and ductile failure (Parisio et al. 2018a). All models have been implemented into the open-source finite element framework OpenGeoSys (Kolditz et al. 2012) which can be found at <https://github.com/ufz/ogs>.

The article is structured as follows: in Sect. 2, the basic mechanical setting is described to set the scene, followed by the introduction of the three methods along with relevant literature in Sects. 3, 4 and 5. In Sect. 6, the parameterization of the different methods based on the same set of experimental data is discussed along with the quantification of key physical properties in the smeared approaches. Fracture volume and fluid mass balance computations are described in Sect. 7 along with the general numerical solution algorithms. Due to the focus on the above mentioned quantities, the simplifying assumption of a toughness-controlled regime with negligible fluid dissipation could be made. As such, fluid pressure is taken as a constant along the fault. Based on this assumption, the numerical solutions are compared with each other and verified against analytical solutions in Sect. 8. Final conclusions are drawn in Sect. 9.

2 General remarks on the mechanical setting

Consider a biphasic setting where a porous solid is fully saturated by a pore fluid and occupies the domain Ω . Embedded in Ω is a domain of co-dimension 1 representing the fracture. The displacement field of the porous solid denoted by $\mathbf{u} \in H^1(\Omega \setminus \Gamma_c; \mathbb{R}^n)$ has a jump across this embedded discontinuity surface Γ_c . Within the matrix, the material's deformation can be expressed by the linearized small strain tensor $\boldsymbol{\epsilon} = \text{sym grad } \mathbf{u}$, provided the displacement gradients remain sufficiently small. Following Biot's theory (Biot 1941), the total Cauchy stress tensor $\boldsymbol{\sigma}$ can be decomposed¹ into the effective stress tensor $\boldsymbol{\sigma}'$ and a contribution due to the pore-pressure p weighted by Biot's coefficient α

$$\boldsymbol{\sigma} = \boldsymbol{\sigma}' - \alpha p \mathbf{I}. \quad (1)$$

The effective stress follows from the material's constitutive relation $\boldsymbol{\sigma}' = \mathbf{C}(\boldsymbol{\epsilon})$. In the intact part of the medium, quasi-static equilibrium demands

$$\text{div } \boldsymbol{\sigma} + \varrho \mathbf{b} = \mathbf{0} \quad \text{in } \Omega \setminus \Gamma, \quad (2)$$

where \mathbf{b} denotes an applied specific body force and ϱ is the mass density of the porous medium. On the Dirichlet part $\partial_D \Omega$ of the domain boundary $\partial \Omega$, fixed displacement boundary conditions are considered,

$$\mathbf{u} = \bar{\mathbf{u}} \quad \text{on } \partial_D \Omega, \quad (3)$$

while a traction $\bar{\mathbf{t}}$ is applied of the remaining part $\partial_N \Omega := \partial \Omega \setminus \partial_D \Omega$.

$$\boldsymbol{\sigma} \mathbf{n} = \bar{\mathbf{t}} \quad \text{on } \partial_N \Omega, \quad (4)$$

In addition to the equilibrium conditions within the uncracked domain, the stress field across the discontinuity Γ_c has to satisfy mechanical equilibrium as well. Let Γ^+ and Γ^- represent the opposing faces of cracks which coincide in the reference configuration and are therein designated as Γ_c ; \mathbf{n}_Γ^\pm denote the outer unit normal to Ω on Γ^\pm respectively. On Γ^\pm , the tractions caused by the fluid pressure in the crack p_f are $-p_f \mathbf{n}_\Gamma^\pm$, so that admissible stress fields satisfy the conditions

$$\boldsymbol{\sigma} \mathbf{n}_\Gamma^\pm = -p_f \mathbf{n}_\Gamma^\pm \quad \text{on } \Gamma^\pm. \quad (5)$$

The displacement discontinuity will subsequently be treated by three different approaches: a strong discontinuity approach based on a cohesive zone model using lower-dimensional (i.e. co-dimension 1) interface elements with local enrichment of the displacement field (Sect. 3); and two approaches in which the discontinuity is smeared over a zone characterized by a length-scale parameter: phase-field models of brittle fracture (Sect. 4) and non-local elasto-plastic damage models (Sect. 5). The basic conceptual ideas of the three models are compared in Fig. 1.

¹ Using the sign convention of solid mechanics.

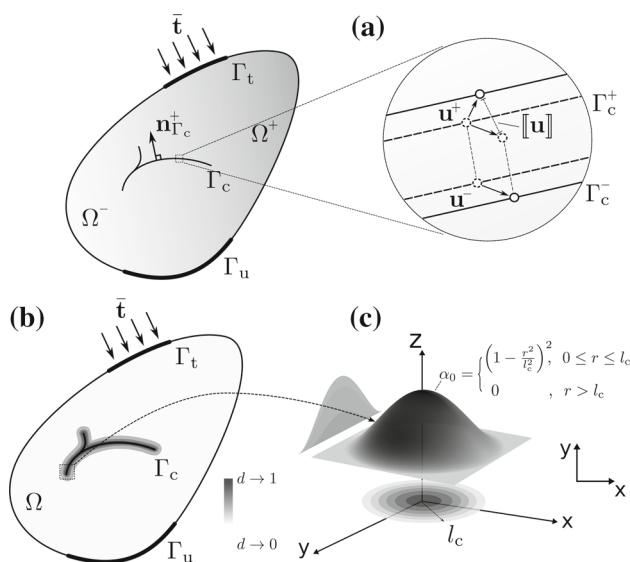


Fig. 1 Conceptual illustration of **a** cohesive zone model using lower-dimensional interface elements with local enrichment to represent a strong displacement discontinuity; **b** phase-field models of brittle fracture in which a crack surface density per unit volume is introduced for regularisation; and **c** non-local elasto-plastic damage models, in which a kernel function with a specified support region is used to characterize a fracture process zone. All models are implemented in OpenGeoSys

The fluid pressure in both matrix and fracture usually follows from the solution of a mass balance equation. In the sequel, the matrix will be considered impermeable and a mass balance only has to be solved for the crack domain. This is done differently for each of the three methods and will be explained in Sect. 7.

3 Lower-dimensional cohesive interface elements with local enrichment

The following implementation is based on Watanabe et al. (2012) and represents a special case of extended finite element methods (Moës et al. 1999; Belytschko et al. 2009, 2001) in that the enrichment is limited to element boundaries. The implementation is here extended to cohesive zone traction separation laws, cf. (Needleman 1990a, b; Nguyen et al. 2001; Elices et al. 2002; Gasser and Holzpfel 2005; Meschke et al. 2007).

3.1 Weak form

The weak form of the static equilibrium equation (2) can be written as the principle of virtual work

$$\int_{\Omega \setminus \Gamma_c} \delta \epsilon : \sigma \, d\Omega - \int_{\Omega \setminus \Gamma_c} \delta \mathbf{u} \cdot \mathbf{b} \, d\Omega - \int_{\partial_N \Omega} \delta \mathbf{u} \cdot \bar{\mathbf{t}} \, d\Gamma - \int_{\Gamma_c} \underbrace{(\delta \mathbf{u}^+ - \delta \mathbf{u}^-) \cdot \mathbf{t}_c}_{\delta [\![\mathbf{u}]\!] } \, d\Gamma = 0, \quad (6)$$

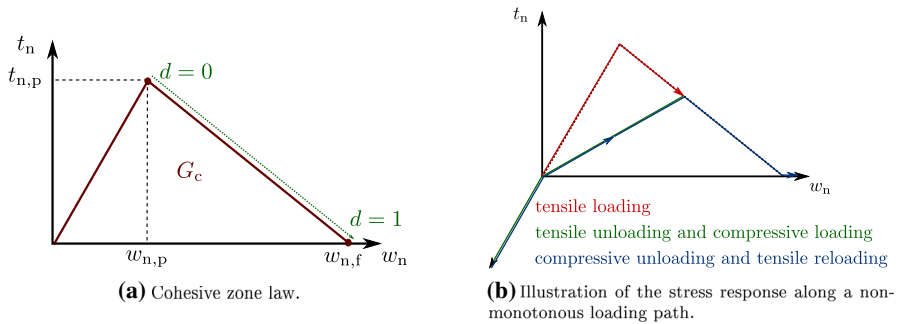


Fig. 2 Cohesive zone model for mode I fracture. Definition of basic parameters (a) and illustration of cleavage unloading, undamaged compressive loading and damaged reloading

where $\delta \mathbf{u}$ is the first variation of the displacement field (virtual displacements), \mathbf{u}^+ and \mathbf{u}^- denote displacements of the opposing fracture phases such that $[\![\mathbf{u}]\!] = \mathbf{u}^+ - \mathbf{u}^-$ is the displacement jump across the interface, $\bar{\mathbf{t}}$ and \mathbf{t}_c are the boundary ($\partial_N \Omega$) and the interface (Γ_c) traction, respectively. While the boundary traction $\bar{\mathbf{t}}$ is given by the applied external forces along the contour, the interface traction \mathbf{t}_c follows from a constitutive response of the interface according to the relative displacement between the opposing surfaces. Note, that the above definition implies stress continuity between the matrix compartments across the interface, viz. Eq. (5), $\mathbf{t}_c = \boldsymbol{\sigma}(\mathbf{x}_\Gamma) \mathbf{n}_\Gamma^+ = -\boldsymbol{\sigma}(\mathbf{x}_\Gamma) \mathbf{n}_\Gamma^-$.

3.2 Constitutive model

While the matrix material behaves according to linear elasticity and is assumed to be impermeable in the current study, the crack will be fluid saturated and follows an effective stress-type formulation:

$$\mathbf{t}_c = \mathbf{t}'_c - p_f \mathbf{n}_\Gamma, \quad (7)$$

where the fluid pressure in the fault only acts on the normal traction across the fault, not its shear components. For the effective stress, a cohesive-zone law has been implemented based on the following assumptions:

- Damage is driven by fracture opening $[\![\mathbf{u}]\!] \cdot \mathbf{n}_\Gamma$ only, i.e. only mode I fracture propagation is considered.
- The traction-separation law is bilinear (Fig. 2a).
- Cleavage unloading (in contrast to ductile unloading) is considered in view of modelling brittle fracture (Fig. 2b).

The cohesive zone model is characterized by its peak tensile normal traction or normal tensile strength $t_{n,p}$, its initial normal and shear stiffness K_n , K_s , and its fracture toughness/critical energy release rate G_c .

The undamaged elastic fracture constitutive law

$$\mathbf{t}'_c = \mathbf{K}[\![\mathbf{u}]\!] = [K_n(\mathbf{n}_\Gamma \otimes \mathbf{n}_\Gamma) + K_s(\mathbf{I} - \mathbf{n}_\Gamma \otimes \mathbf{n}_\Gamma)] [\![\mathbf{u}]\!], \quad (8)$$

remains valid in compression ($w_n = [\mathbf{u}] \cdot \mathbf{n}_r < 0$). During compressive loading, a penalty formulation

$$K_n^{\text{pen}} = K_n \left[1 + \ln^2 \left(\frac{b}{b_0} \right) \right], \quad (9)$$

based on current (b) and initial (b_0) aperture is invoked to prevent fracture face interpenetration at high compressive loads.

In tension, the model is modified to account for damage

$$\mathbf{t} = \mathbf{K}^d [\mathbf{u}]. \quad (10)$$

During monotonously increasing loading, damage evolves linearly with normal fault opening between the limiting values

$$d = \begin{cases} 0 & w_n = w_{n,p} \\ 1 & w_n = w_{n,f}, \end{cases} \quad (11)$$

where $w_{n,p} = \frac{t_{n,p}}{K_n}$ and $w_{n,f} = 2 \frac{G_c}{t_{n,p}}$.

Damage is implemented as a non-decreasing function according to:

$$d^{t+\Delta t} = \min \left[1, \max \left(\frac{\langle w - w_{n,p} \rangle}{w_{n,f} - w_{n,p}}, d^t \right) \right], \quad (12)$$

where the Macauley brackets have been used.

The new tensile normal stiffness is found via

$$K_n^d = \frac{t_n}{w_n} = \frac{(1-d)t_{n,p}}{\max_{0 \leq \tau \leq t} w_n(\tau)} = \frac{(1-d)K_n w_{n,p}}{d(w_{n,f} - w_{n,p}) + w_{n,p}}. \quad (13)$$

Accordingly, the entire stiffness tensor is degraded:

$$\mathbf{K}^d = \frac{(1-d)w_{n,p}}{d(w_{n,f} - w_{n,p}) + w_{n,p}} \mathbf{K} = g(d)\mathbf{K}. \quad (14)$$

In case of $d^{t+\Delta t} > d^t$ within the employed incremental-iterative solution scheme, the algorithmic tangent \mathbf{D} is extended by a second term:

$$\mathbf{D} = \mathbf{K}^d + \mathbf{K} [\mathbf{u}] \otimes \frac{\partial g(d)}{\partial d} \frac{\partial d}{\partial [\mathbf{u}]}, \quad (15)$$

$$\text{with } \frac{\partial d}{\partial w_n} = \frac{1}{w_{n,f} - w_{n,p}} \quad \text{and} \quad \frac{\partial g(d)}{\partial d} = -\frac{w_{n,p}w_{n,f}}{[d(w_{n,f} - w_{n,p}) + w_{n,p}]^2}. \quad (16)$$

Since the matrix was considered impermeable, a fluid pressure was only required in the cracked domain. For that purpose, Eq. (7) was modified to read:

$$\mathbf{t}_c = \mathbf{t}'_c - dp_f \mathbf{n}_\Gamma \quad (17)$$

The determination of p_f is described in Sect. 7.

3.3 Numerical implementation

The implementation within an extrinsically enriched finite element scheme follows Watanabe et al. (2012). In addition to the usual nodal displacement degrees of freedom for continuous settings, nodal degrees of freedom equivalent to the displacement jump are introduced as additional unknowns. Hence, in contrast to the other methods used in this paper, the displacement jump is explicitly given as a primary solution of the enriched finite element scheme such that the displacement solution displays a strong discontinuity. Non-linearities are linearized using an incremental iterative Newton–Raphson method resulting in a linear system

$$\begin{bmatrix} \mathbf{K}_{uu} & \mathbf{K}_{ua} \\ \mathbf{K}_{au} & \mathbf{K}_{aa} \end{bmatrix} \begin{Bmatrix} \Delta \mathbf{u} \\ \Delta \mathbf{a} \end{Bmatrix} = \begin{Bmatrix} \mathbf{f}_u^{\text{ext}} \\ \mathbf{f}_a^{\text{ext}} \end{Bmatrix} - \begin{Bmatrix} \mathbf{f}_u^{\text{int}} \\ \mathbf{f}_a^{\text{int}} \end{Bmatrix},$$

which is solved until convergence is achieved. Here, $\Delta \mathbf{u}$ and $\Delta \mathbf{a}$ denote the increments of the regular nodal displacement and the additional degrees of freedom related to the displacement jump across the interface, $\mathbf{K}_{\bullet\bullet}$ are the sub-matrices of the stiffness matrix of the problem and the right-hand-side consists of the out-of-balance (residual) force vectors.

4 Phase-field model of brittle fracture

Phase-field modelling has emerged as one of the most appealing numerical techniques for simulation of fracture in the last two decades. A widely applied approach of phase-field models of fracture was first introduced by Bourdin et al. (2000) as a numerical implementation method to the variational approach to fracture proposed by Francfort and Marigo (1998) using the Γ -convergence properties. Since this inception, the approach has been adapted in many studies ranging from ductile fracture (Ambati et al. 2015; Alessi et al. 2015; Miehe et al. 2016) to hydraulic fracturing (Bourdin et al. 2012; Wheeler et al. 2014; Miehe et al. 2015; Wilson and Landis 2016; Heider and Markert 2016; Chukwudozie 2016; Yoshioka and Bourdin 2016; Santillán et al. 2017) to name a few.

4.1 Regularisation of the total energy functional

Francfort and Marigo (1998) define a total energy functional as the sum of the elastic strain energy, the potential of the external forces and the surface energy as:

$$E(\mathbf{u}, \Gamma_c) := \int_{\Omega \setminus \Gamma_c} \psi(\mathbf{u}) \, d\Omega - \int_{\partial_N \Omega} \bar{\mathbf{t}} \cdot \mathbf{u} \, d\Gamma - \int_{\Omega \setminus \Gamma_c} \varrho \mathbf{b} \cdot \mathbf{u} \, d\Omega + G_c \mathcal{H}^{N-1}(\Gamma_c), \quad (18)$$

where \mathcal{H} is the Hausdorff measure. For the extension to hydraulic fracturing, the work done by the fluid pressure on crack faces $\int_{\Gamma_c} p[[\mathbf{u}]] \cdot \mathbf{n}_\Gamma \, d\Gamma$ is added to the total energy which can now be written as

$$E(\mathbf{u}, \Gamma_c) := \int_{\Omega \setminus \Gamma_c} \psi(\mathbf{u}) \, d\Omega - \int_{\partial_N \Omega} \bar{\mathbf{t}} \cdot \mathbf{u} \, d\Gamma - \int_{\Omega \setminus \Gamma_c} \varrho \mathbf{b} \cdot \mathbf{u} \, d\Omega + G_c \mathcal{H}^{N-1}(\Gamma_c) + \int_{\Gamma_c} p[[\mathbf{u}]] \cdot \mathbf{n}_\Gamma \, d\Gamma. \quad (19)$$

Bourdin et al. (2000) introduced a phase-field variable to regularise the functional adapting the Γ -convergence result obtained in Ambrosio and Tortorelli (1990) and the total energy functional takes the following form (Bourdin et al. 2014; Marigo et al. 2016):

$$E(\mathbf{u}, d) := \int_{\Omega} \psi(\mathbf{u}, d) \, d\Omega - \int_{\partial_N \Omega} \bar{\mathbf{t}} \cdot \mathbf{u} \, d\Gamma - \int_{\Omega} \varrho \mathbf{b} \cdot \mathbf{u} \, d\Omega + \frac{G_c}{4c_w} \int_{\Omega} \left(\frac{w(d)}{\ell} + \ell |\nabla d|^2 \right) d\Omega + \int_{\Gamma_c} p[[\mathbf{u}]] \cdot \mathbf{n}_\Gamma \, d\Gamma, \quad (20)$$

where d is the damage variable that equals 0 when undamaged and 1 for a fully damaged state. $\psi(\mathbf{u}, d)$ is the degraded strain energy density, and w is a dissipated energy function such that $\psi(\mathbf{u}, 0) = \psi(\mathbf{u})$ and $w(0) = 0$ and $\psi(\mathbf{u}, 1) = 0$ and $w(1) = 1$ are ensured. The most popular choice for the degradation function is a quadratic form, $\psi(\mathbf{u}, d) = (1 - d)^2 \psi(\mathbf{u})$, which is used in this study, while other higher-order polynomial functions were also considered in literature (Karma et al. 2001; Borden et al. 2012). G_c is the fracture surface energy, c_w is a normalization parameter defined as $c_w := \int_0^1 \sqrt{w(s)} ds$, and ℓ is a regularisation length. Various possible dissipative energy functions w are discussed in Marigo et al. (2016). The most widely used function is a quadratic form (Kuhn and Müller 2010; Miehe et al. 2010; Klinsmann et al. 2015) for which Eq. (20) is given by

$$E(\mathbf{u}, d) := \int_{\Omega} (1 - d)^2 \psi(\mathbf{u}) \, d\Omega - \int_{\partial_N \Omega} \bar{\mathbf{t}} \cdot \mathbf{u} \, d\Gamma - \int_{\Omega} \varrho \mathbf{b} \cdot \mathbf{u} \, d\Omega + \frac{G_c}{2} \int_{\Omega} \left(\frac{d^2}{\ell} + \ell |\nabla d|^2 \right) d\Omega + \int_{\Gamma_c} p[[\mathbf{u}]] \cdot \mathbf{n}_\Gamma \, d\Gamma. \quad (21)$$

This regularised Eq. (21) is called AT2 model in Bourdin et al. (2014) and Tanné et al. (2018) after Ambrosio and Tortorelli (1990, 1992), and this terminology is adopted in the present study. Another choice for $w(d)$ is a linear form called AT1 introduced in Bourdin et al. (2014) following Braides (1998, Sect. 3.2) for which Eq. (20) is consequently given as

$$\begin{aligned}
 E(\mathbf{u}, d) := & \int_{\Omega} (1-d)^2 \psi(\mathbf{u}) d\Omega - \int_{\partial_N \Omega} \bar{\mathbf{t}} \cdot \mathbf{u} d\Gamma - \int_{\Omega} \varrho \mathbf{b} \cdot \mathbf{u} d\Omega \\
 & + \frac{3G_c}{8} \int_{\Omega} \left(\frac{d}{\ell} + \ell |\nabla d|^2 \right) d\Omega + \int_{\Gamma_c} p \llbracket \mathbf{u} \rrbracket \cdot \mathbf{n}_{\Gamma} d\Gamma.
 \end{aligned} \quad (22)$$

The work done by the pressure in the crack is still explicitly dependent on the displacement jump and remains to be cast into a continuous setting. In Bourdin et al. (2012), an approximation $\int_{\Omega} p \mathbf{u} \cdot \nabla d d\Omega$ has been proposed to take into account the pressure work, which Γ -converges to $\int_{\Gamma_c} p \llbracket \mathbf{u} \rrbracket \cdot \mathbf{n}_{\Gamma} d\Gamma$. Using this approximation, Eq. (20) can be written in its now fully regularised form

$$\begin{aligned}
 E(\mathbf{u}, d, p) = & \int_{\Omega} (1-d)^2 \psi(\mathbf{u}) d\Omega - \int_{\partial_N \Omega} \bar{\mathbf{t}} \cdot \mathbf{u} d\mathbf{s} - \int_{\Omega} \varrho \mathbf{b} \cdot \mathbf{u} d\Omega \\
 & + \frac{G_c}{4c_w} \int_{\Omega} \left(\frac{w(d)}{\ell} + \ell |\nabla d|^2 \right) d\Omega + \int_{\Omega} p \mathbf{u} \cdot \nabla d d\Omega.
 \end{aligned} \quad (23)$$

While it was proposed to split the strain energy term, $\int_{\Omega} (1-d)^2 \psi(\mathbf{u}) d\Omega$, to take into account the possibility of crack closure into a degraded part and an undegradable (usually compressive) part (Amor et al. 2009; Freddi and Royer-Carfagni 2010; Miehe et al. 2010) as $\int_{\Omega} (1-d)^2 \psi(\mathbf{u}) d\Omega = \int_{\Omega} [(1-d)^2 \psi^+(\mathbf{u}) + \psi^-(\mathbf{u})] d\Omega$, the choice of the split remains an open question (Li et al. 2016). In the examples shown in the subsequent sections, the symmetric model is used to be consistent with the closed-form solutions.

4.2 Numerical implementation

The solution of Eq. (23) follows the alternate minimisation scheme introduced in Bourdin et al. (2000) with respect to \mathbf{u} and d given a time-evolving volume constraint $V_{\text{inj}} = V_{\text{crack}} (= \int_{\Omega} \mathbf{u} \cdot \nabla d d\Omega)$.² The functional is cast into a dimensionless format before application of the alternating minimization scheme (see “Appendix A”) to avoid ill-posedness that may be caused by input parameter units Chukwudozie (2016). Thus, the minimisation problem can be stated as

$$\begin{aligned}
 (\tilde{\mathbf{u}}, d, \tilde{p})^* = & \arg \min \tilde{E}(\tilde{\mathbf{u}}, d, \tilde{p}), \\
 & \begin{cases} \tilde{\mathbf{u}} \in H^1 \\ d \in H^1, d^t \subset d^{t+\Delta t} \\ \tilde{V} = \int_{\Omega} \tilde{\mathbf{u}} \cdot \nabla d d\Omega \end{cases}
 \end{aligned} \quad (24)$$

where $\tilde{V}_{\text{crack}} = u_0 x_0^{n-1} V$ and irreversibility of d is enforced as in Bourdin et al. (2000). The first variation of the energy functional with respect to \mathbf{u} is

² This constraint can also be added to the functional and its Lagrange multiplier turns out to be exactly the pressure (Chukwudozie 2016).

$$\begin{aligned} \delta \tilde{E}(\mathbf{u}, d, p; \delta \mathbf{u}) = & \frac{1}{2} \int_{\Omega} (1-d)^2 \tilde{\mathbf{C}}(\boldsymbol{\epsilon}(\tilde{\mathbf{u}})) : \boldsymbol{\epsilon}(\delta \tilde{\mathbf{u}}) \, d\Omega - \\ & - \int_{\partial_N \Omega} \tilde{\mathbf{t}} \cdot \delta \tilde{\mathbf{u}} \, d\Gamma - \int_{\Omega} \varrho \tilde{\mathbf{b}} \cdot \delta \tilde{\mathbf{u}} \, d\Omega + \int_{\Omega} \tilde{p} \delta \tilde{\mathbf{u}} \cdot \nabla d \, d\Omega, \end{aligned} \quad (25)$$

where $\tilde{\mathbf{C}}$ is the constitutive relation that satisfies $\psi = \tilde{\mathbf{C}}(\boldsymbol{\epsilon}) : \boldsymbol{\epsilon}/2$. In the present study, isotropic linear elasticity was used: $\psi = \boldsymbol{\epsilon} : \mathbf{C} : \boldsymbol{\epsilon}/2$. The first variation of the energy functional with respect to d for the *AT1* model is given as

$$\begin{aligned} \delta \tilde{E}(\mathbf{u}, d, p; \delta d) = & - \int_{\Omega} d \delta d \tilde{\mathbf{C}}(\boldsymbol{\epsilon}(\tilde{\mathbf{u}})) : \boldsymbol{\epsilon}(\tilde{\mathbf{u}}) \, d\Omega \\ & + \frac{3G_c}{8} \int_{\Omega} \left(\frac{\delta d}{\ell} + 2\ell \nabla d \cdot \nabla \delta d \right) \, d\Omega + \int_{\Omega} \tilde{p} \tilde{\mathbf{u}} \cdot \nabla \delta d \, d\Omega, \end{aligned} \quad (26)$$

and for the *AT2* model as

$$\begin{aligned} \delta \tilde{E}(\mathbf{u}, d, p; \delta d) = & - \int_{\Omega} d \delta d \tilde{\mathbf{C}}(\boldsymbol{\epsilon}(\tilde{\mathbf{u}})) : \boldsymbol{\epsilon}(\tilde{\mathbf{u}}) \, d\Omega \\ & + G_c \int_{\Omega} \left(\frac{d}{\ell} \delta d + \ell \nabla d \cdot \nabla \delta d \right) \, d\Omega + \int_{\Omega} \tilde{p} \tilde{\mathbf{u}} \cdot \nabla \delta d \, d\Omega. \end{aligned} \quad (27)$$

Note that d represents the state of the material constrained in $[0, 1]$ and that this constraint is automatically fulfilled with *AT2* in pure mechanical settings whereas only *AT1* requires the solution of a variational inequality. As can be seen in the above extension to hydraulic fracturing, however, both *AT1* and *AT2* models now require enforcement of the variational inequality ($0 \leq d \leq 1$) due to the presence of the pressure-work term in the energy functional. In this study, a variational inequality non-linear solver of the PETSc library (Balay et al. 1997, 2017a, b) has been applied to satisfy the constraint on d .

5 Non-local integral formulation of elasto-plasticity with damage

5.1 Constitutive model

The theory of continuum damage mechanics has been consistently and successfully applied to the simulation of failure and fracture of brittle and ductile solids in the spirit of the local approach to fracture (Lemaitre et al. 2009; Murakami 2012). Because of the softening response, continuum damage models suffer from spurious mesh-dependency: the rate equation of equilibrium loses ellipticity, the acoustic tensor becomes singular and the problem ill-posed, bifurcated solutions of the static equilibrium might appear and the global dissipated energy decreases upon mesh-element size decrement. In the extreme case, snap-backs are possible and a cusp-catastrophe surface appears in the three-dimensional stress versus strain versus element-size space. Restoring objectivity in the solution with respect to mesh size has often been achieved by introducing an internal length in what is usually referred to as an extended or non-local

continuum. In this contribution, we employ an integral-type non-local plastic-damage model, which can successfully prevent ill-posedness of the rate problem for softening damage models (Bazant and Jirasek 2002; Duddu and Waisman 2013; Nguyen et al. 2015; Desmorat et al. 2015; Parisio et al. 2018a). The constitutive equation of the plastic-damage model relates Biot's effective stress to the elastic strain tensor as

$$\boldsymbol{\sigma}' = \tilde{\mathcal{C}} : \boldsymbol{\epsilon}_{\text{el}}, \quad (28)$$

where $\tilde{\mathcal{C}} = (1 - d) \mathcal{C}$ is the damaged elastic tensor,³ $0 \leq d \leq 1$ is the damage parameter, $\boldsymbol{\epsilon}_{\text{el}}$ is the elastic strain tensor defined as the difference between total and plastic strain

$$\boldsymbol{\epsilon}_{\text{el}} = \boldsymbol{\epsilon} - \boldsymbol{\epsilon}_{\text{pl}}. \quad (29)$$

According to Eq. (28), the concept of damage effective stress can be defined as the stress that acts on the undamaged part of the material as

$$\tilde{\boldsymbol{\sigma}} = \frac{\boldsymbol{\sigma}'}{1 - d} = \mathcal{C} : \boldsymbol{\epsilon}_{\text{el}}. \quad (30)$$

The loading surface for this class of plastic-damage model can be chosen as unique for the two dissipative mechanisms. In this case, we will employ a J_2 -type failure surface of the Drucker–Prager family formulated in the damage effective stress space $\tilde{\boldsymbol{\sigma}}$:

$$F = \sqrt{J_2} - \beta I_1 + k = 0, \quad (31)$$

with β and k material parameters and the invariants of the stress tensor defined as

$$I_1 = \text{tr}(\tilde{\boldsymbol{\sigma}}), \quad J_2 = (\tilde{\mathbf{s}} : \tilde{\mathbf{s}}) / 2, \quad (32)$$

where $\tilde{\mathbf{s}} = \tilde{\boldsymbol{\sigma}} - \text{tr}(\tilde{\boldsymbol{\sigma}}) / 3 \mathbf{I}$ is the deviatoric effective stress tensor. The Karush–Kuhn–Tucker loading-unloading conditions write

$$F(\tilde{\boldsymbol{\sigma}}) \leq 0 \quad \lambda \geq 0 \quad \lambda F(\tilde{\boldsymbol{\sigma}}) = 0, \quad (33)$$

with λ the plastic multiplier that defines the plastic strain rate as

$$\dot{\boldsymbol{\epsilon}}_{\text{pl}} = \lambda \frac{\partial G}{\partial \tilde{\boldsymbol{\sigma}}}, \quad (34)$$

In the current study, associated plasticity was modelled, i.e. the plastic potential function G was identical to the yield function $G = F$.

³ Observe the linear degradation of stiffness in comparison to the quadratic formulation used in the phase-field formulation. Consequences of this choice have been discussed in de Borst and Verhoosel (2016b) where gradient-damage and phase-field models were compared. For links on non-local integral formulations and gradient-damage models, the reader is referred to Kuhl et al. (2000) and references therein.

A non-local damage-driving variable \bar{k}_d is obtained by integral averaging of its local counterpart k_d

$$\bar{k}_d(\mathbf{x}) = \frac{1}{\int_V \alpha_0(\|\mathbf{x} - \boldsymbol{\psi}\|) d\boldsymbol{\psi}} \int_V \alpha_0(\|\mathbf{x} - \boldsymbol{\xi}\|) k_d(\boldsymbol{\xi}) d\boldsymbol{\xi}, \quad (35)$$

where $r = \|\mathbf{x} - \boldsymbol{\xi}\|$ is the distance between two points in the continuum and α_0 is the weight function (compare Fig. 1)

$$\alpha_0 = \begin{cases} \left(1 - \frac{r^2}{l_c^2}\right) & \text{if } 0 \leq r \leq l_c \\ 0 & \text{if } l_c \leq r \end{cases}. \quad (36)$$

In Eq. (36), l_c is an internal length of the continuum which defines the radius of interaction of the different points in the material. For the theoretical justification and the relation of l_c with internal micro-structural characteristics, the interested reader is addressed to consult the literature (Bazant and Jirasek 2002). The local damage-driving variable k_d of Eq. (35) is in turn a function of the rate of effective plastic strain and is defined in rate form as

$$\dot{k}_d = \dot{\epsilon}_{\text{pl}}^{\text{eff}} \quad (37)$$

with

$$\epsilon_{\text{pl}}^{\text{eff}}(t) = \int_0^t \sqrt{\frac{2}{3} \dot{\epsilon}_{\text{pl}} : \dot{\epsilon}_{\text{pl}}} d\tau. \quad (38)$$

Finally, damage d is an exponential function of the non-local driving variable as \bar{k}_d

$$d = \omega(\bar{k}_d) = 1 - \exp\left(-\frac{\bar{k}_d}{\alpha_d}\right), \quad (39)$$

where α_d is a material parameter controlling the rate of damage growth, and therefore material brittleness (Parisio and Laloui 2017).

As the matrix was considered impermeable, a fluid pressure was only required in the damaged domain. For that purpose, Eq. (1) was modified to read

$$\boldsymbol{\sigma} = \boldsymbol{\sigma}' - dp\mathbf{I}. \quad (40)$$

The determination of p is described in Sect. 7.

5.2 Numerical implementation

The solution of the differential-algebraic system of equations describing the plastic-damage model is performed at each integration point within a fully implicit scheme for non-linear materials (Parisio et al. 2015; Nagel et al. 2016, 2017; Parisio et al.

2018b). Because of the adopted coupling between damage and plasticity, damage can be explicitly computed and updated after the return-mapping algorithm has solved the plastic sub-problem in damage effective-stress space. The Newton–Raphson method for the plastic problem minimizes the residual $\mathbf{R}(\mathbf{z})$, which is a function of the vector of state variables \mathbf{z} .

The sought state variable vector contains the solution of the plastic problem at time step $t + \Delta t$ in terms of damage effective stress $\tilde{\sigma}^{t+\Delta t}$, plastic strain $\epsilon_{\text{pl}}^{t+\Delta t}$ and plastic multiplier $\lambda^{t+\Delta t}$. The residual to be minimized associated with the plastic state variables contains the equations of stress, plastic strain rate and the yield surface as an algebraic constraint and is expressed as

$$\mathbf{R}(\mathbf{z}) = \begin{cases} \tilde{\sigma}^{t+\Delta t} - \mathbf{C}(\epsilon^{t+\Delta t} - \epsilon_{\text{pl}}^{t+\Delta t}) \\ \epsilon_{\text{pl}}^{t+\Delta t} - \epsilon_{\text{pl}}^t - \Delta t \lambda^{t+\Delta t} \frac{\partial G}{\partial \tilde{\sigma}^{t+\Delta t}} \\ F(\tilde{\sigma}^{t+\Delta t}) \end{cases} \quad (41)$$

Linearization of the residual with respect to the state variables yields the following iterative Newton–Raphson scheme

$$\mathbf{z}_{n+1}^{t+\Delta t} = \mathbf{z}_n^{t+\Delta t} - (\mathbf{J}_n^{t+\Delta t})^{-1} \mathbf{R}_n^{t+\Delta t}, \quad (42)$$

with the Jacobian

$$\mathbf{J}_n^{t+\Delta t} = \left. \frac{\partial \mathbf{R}^{t+\Delta t}}{\partial \mathbf{z}^{t+\Delta t}} \right|_n, \quad (43)$$

which can be computed analytically (as in the present case) or using a numerical perturbation technique. The process is iterated over n until $\|\mathbf{R}\| < \theta_{\text{tol}}$. The elasto-plastic tangent matrix \mathbf{C}_{pl} is extracted from the Jacobian by solving the following system after local convergence

$$\frac{d\mathbf{z}}{d\epsilon} = -\mathbf{J}^{-1} \frac{\partial \mathbf{R}}{\partial \epsilon}, \quad (44)$$

where the first entries of \mathbf{z} contain $\tilde{\sigma}$ (Nagel et al. 2017). The non-local damage variable \bar{k}_d can be computed explicitly after convergence of the plastic algorithm, and is approximated in the finite element scheme as

$$\bar{k}_{d,i} = \frac{\sum_{j=1}^{n_p} w_j \alpha_0 (\|\mathbf{x}_i - \mathbf{x}_j\|) k_d(\mathbf{x}_j) \det J(\mathbf{x}_j)}{\sum_{k=1}^{n_p} w_k \alpha_0 (\|\mathbf{x}_i - \mathbf{x}_k\|) \det J(\mathbf{x}_k)}, \quad (45)$$

where n_p is the number of integration points, $\det J(\mathbf{x}_k)$ is the determinant of the Jacobian of the isoparametric element coordinate transformation. The integration scheme is run on the integration points that fall into the non-local interaction radius l_c . From $\bar{k}_{d,i}$, damage at integration points is computed from Eq. (39).

6 Material properties

Before comparing simulation results based on the three model formulations, inter-model consistency in terms of parametrization has to be ensured in face of the different mathematical and physical concepts underlying the models. The calibration procedures for the three models are therefore briefly illustrated in the following sections, relations to spatial discretization discussed, and then applied to represent an anisotropic pink Gneiss from the Erzgebirge mountain range in Saxony, Germany (personal communication from Thomas Frühwirth and Heinz Konietzky; cf. Acknowledgements).

6.1 Rock properties

The properties of the Gneiss are taken only according to one configuration of the foliation planes, so that the material is finally considered isotropic. The density is $\varrho = 2.68 \text{ g cm}^{-3}$, Young's modulus $E = 80 \text{ GPa}$, Poisson's ratio $\nu = 0.15$, uniaxial compressive strength $\sigma_c = 120\text{--}160 \text{ MPa}$, uniaxial tensile strength $\sigma_t = 6\text{--}17 \text{ MPa}$ and fracture energy $G_c = 20 \text{ Pa m}$. Each model is calibrated based on E , ν , and G_c ; additional properties to complete the model description are quantified from, e.g., the tensile σ_t and compressive strengths σ_c , as discussed below.

6.2 Cohesive zone traction-separation law

The tensile strength $t_{n,p}$ and critical energy release rate G_c required to parameterize the failure behaviour of the cohesive zone model, cf. Eq. (11), can be taken directly from the above set of experimentally determined material parameters. The determination of the initial normal stiffness K_n in Eq. (11) may proceed from the intrinsic mechanical properties of the matrix material as well as the geometry of a potential pre-existing fault, see also (Oliver 2000; Oliver et al. 2002). Therefore, the setting of the normal stiffness can be estimated as follows

$$K_n = \frac{E}{b_0} \geq \frac{t_{n,p}^2}{2G_c}. \quad (46)$$

In general and if no pre-existing fault is modelled, however, K_n can be set independently and controls the brittleness of failure and the magnitude of elastic opening before failure. The lower limit corresponds to the extreme case in which sudden brittle breakage occurs once the normal tensile strength is mobilised. For numerical reasons, K_n was herein set to $10^{14} \text{ MPa m}^{-1}$, which is several orders of magnitude higher than the lower limit $K_{n,\min} \approx 10^7 \text{ MPa m}^{-1}$ in case of $\sigma_t = 17 \text{ MPa}$.

The choice of material parameters introduces a cohesive zone process length l_{cz} characterizing the spread of the failure zone. This length has the form (Hillerborg et al. 1976; Rice 1979)

$$l_{cz} = E \frac{G_c}{t_{n,p}^2}. \quad (47)$$

In order to resolve the failure process numerically, sufficient discretization is required (Davila et al. 2001; Moës and Belytschko 2002). Turon et al. (2007) suggested the total number of interface elements across the cohesive zone length might be as many as 3.

6.3 Phase-field: effective fracture energy and effective crack length

The phase-field approach in principle only requires E , ν , and G_c in the material description, whereas ℓ was originally introduced as a numerical regularisation parameter in view of Γ -convergence. However, recent studies of Marigo et al. (2016) and Zhang et al. (2017) suggest that ℓ be treated as an internal length, i.e. a material property. Given the uniaxial tensile strength, σ_t , the internal length can be obtained as follows (Tanné et al. 2018)

$$\sigma_t = \begin{cases} \sqrt{\frac{3G_c E'}{8\ell}} & \text{for AT1} \\ \frac{3}{16} \sqrt{\frac{3G_c E'}{\ell}} & \text{for AT2} \end{cases}. \quad (48)$$

Using the material properties from Sect. 6.1, the internal length for AT1 and AT2 can be computed as 0.017 m and 0.0048 m respectively, which is comparable to the internal length sizes used in this study ranging from 0.00375 to 0.03 m. As investigated by Tanné et al. (2018), as long as the internal length is insignificant with respect to the defect size, which in our case is 0.2 m, the choice of ℓ will have minimum impact on fracture propagation in toughness-dominated settings; similar conclusions were drawn in Klinsmann et al. (2015) and Zhang et al. (2017).

In the phase-field models, the crack “surface” is approximated by

$$S(x, d, \nabla d) := \frac{1}{4c_w} \int_{\Omega} \left(\frac{w(d)}{\ell} + \ell |\nabla d|^2 \right) d\Omega. \quad (49)$$

The optimal profile of the damage field, d can be obtained by taking $\delta S / \delta d = 0$. Thus,

$$\frac{w'(d)}{\ell} - 2\ell \nabla^2 d = 0. \quad (50)$$

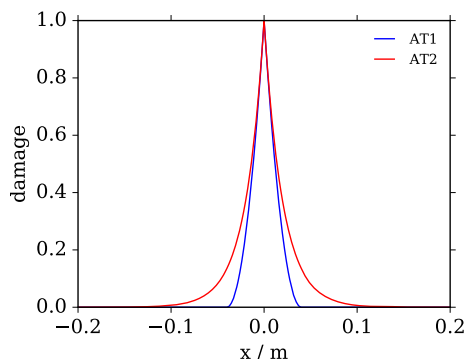
For AT1, $w(d) = d$. Therefore, the optimal profile is given by

$$d(x) = \begin{cases} \left(1 - \frac{|x - x_0|}{2\ell} \right)^2, & \text{for } |x - x_0| \leq 2\ell \\ 0, & \text{otherwise} \end{cases} \quad (51)$$

and for AT2, $w(d) = d^2$, it is

$$d(x) = \exp \left(-\frac{|x - x_0|}{\ell} \right). \quad (52)$$

Fig. 3 Optimal damage profiles for AT1 and AT2



where x_0 is the crack location. The optimal profiles of the damage field for AT1 and AT2 are plotted in Fig. 3.

Provided that Eq. (49) multiplied by G_c represents the surface energy term, the regularised surface energy terms in a discretised domain can be approximated using the optimal profile [Eqs. (51) or (52)]. We consider a line crack with a length of $2a$ centered at the origin ($-a \leq x \leq a$) which lies in an finite domain. Then, the damage profile for AT1 is given by

$$d_h(\xi) = \begin{cases} 1, & \text{for } |x| \leq a, |y| \leq \frac{h}{2} \\ \left(1 - \frac{\xi}{2\ell}\right)^2, & \text{for } \xi \leq 2\ell \\ 0, & \text{otherwise} \end{cases} \quad (53)$$

where h is the discretisation size and ξ is the distance from the crack. The surface energy term can then be approximated from an areal integral

$$\begin{aligned} & \int_{-\infty}^{+\infty} \int_{-\infty}^{+\infty} \frac{3G_c}{8} \left(\frac{d_h}{\ell} + \ell |\nabla d_h|^2 \right) dx dy \\ &= G_c \left(\frac{3h}{8\ell} + 1 \right) a \left[1 + \frac{\pi \ell}{4a(3h/8\ell + 1)} \right] = G_c^{\text{eff}} a^{\text{eff}}. \end{aligned} \quad (54)$$

The first term on the RHS, $G_c(3h/8\ell + 1)$, is known as the effective fracture toughness, G_c^{eff} (Bourdin et al. 2008; Chukwudozie 2016). The second term originates from the damage profile near the crack tip and will be called the effective crack length, a^{eff} , in this study, which can also be estimated using the level-set at certain damage value. Note, that the effective crack length approaches the true crack length a as the crack length (defect size) increases with respect to the internal length, ℓ , unlike the effective fracture toughness which only depends on the discretization with respect to ℓ . Similarly for AT2, the discretised damage profile is given by

$$d_h(\xi) = \begin{cases} 1, & \text{for } |x| \leq a_0, |y| \leq \frac{h}{2} \\ \exp\left(-\frac{\xi}{\ell}\right), & \text{otherwise} \end{cases} \quad (55)$$

Then the effective fracture toughness and crack length can be obtained from

$$\begin{aligned} \int_{-\infty}^{+\infty} \int_{-\infty}^{+\infty} \frac{G_c}{2} \left(\frac{d_h^2}{\ell} + \ell |\nabla d_h|^2 \right) dx dy &= G_c \left(\frac{h}{2\ell} + 1 \right) a \left[1 + \frac{\pi \ell}{4a(h/2\ell + 1)} \right] \\ &= G_c^{\text{eff}} a^{\text{eff}}. \end{aligned} \quad (56)$$

As can be seen in the above equations, the effective fracture surface energy is augmented in the phase-field model to maintain physically adequate dissipation. Therefore, the equivalent G_c^{eff} needs to be provided in the analysis in order to obtain correct results. For example, for $G_c = 20 \text{ Pa m}$, $h = 0.01 \text{ m}$, and $\ell = 0.03 \text{ m}$, the values $G_c^{\text{eff}} = 17.78 \text{ Pa m}$ and $G_c^{\text{eff}} = 17.14 \text{ Pa m}$ have to be provided for *AT1* and *AT2*, respectively, to remain physically equivalent. When comparing crack propagation, the respective formulations for a^{eff} should be employed to ensure equivalence.

6.4 Non-local plastic-damage: volumetric and surface energy density

For the plastic-damage model, the fracture energy in tension (mode I) G_c can be computed from the fracture energy density g_f as

$$G_c = g_f w_t, \quad (57)$$

where w_t is the fracture width, which in this case corresponds to the width of the damaged zone. The fracture energy density in tension can be computed from the total dissipated energy in a uniaxial tensile test performed to failure

$$g_f = \int_0^\infty \sigma(\epsilon) d\epsilon = A_1 + A_2, \quad (58)$$

which can be split into two contributions: a first contribution of elastic energy at peak tensile stress (tensile strength; somewhat analogous to Fig. 2a)

$$A_1 = \frac{\sigma_t^2}{2E}, \quad (59)$$

and a second contribution due to inelastic post-peak dissipation

$$\begin{aligned} A_2 &= \int_{\sigma_t/E}^\infty \sigma(\epsilon) d\epsilon = \int_{\sigma_t/E}^\infty \sigma_t (1 - d) d\epsilon \\ &= \int_{\sigma_t/E}^\infty \sigma_t \exp[-(\epsilon - \sigma_t/E)/\alpha_d] d\epsilon = \alpha_d \sigma_t. \end{aligned} \quad (60)$$

The fracture energy G_c does not explicitly enter the set of parameters of the non-local plastic-damage. Due to the fact that the non-local operator averages an a-priori unknown field (be that damage, strain energy or, as in this case, k_d), the extent of the damaged zone (i.e., the fracture width w_t) is not clearly defined and will depend

upon the problem solved. Furthermore, G_c depends on structural size relative to the internal length, which makes the correlation between global fracture energy in mode I and the internal length l_c a non-trivial task. Often, such correlation is written as a linear dependency (Nguyen and Houlsby 2007; Nguyen et al. 2015)

$$G_c = g_f w_t = g_f \beta_k l_c, \quad (61)$$

where β_k is an empirical coefficient which can take values from 1 to 3 depending on the analysed problem. In the current case, best fit to the fracture energy of $G_c = 20 \text{ Pa m}$ is obtained with a value of $\beta_k = 2.4$. The calibration can be carried out by fixing either σ_t or α_d and the remaining free parameter is obtained by solving Eq. (61) for a fixed G_c . In the current case we have made the assumption that compressive strength is $\sigma_c = 10\sigma_t$, which falls into the range of the experimentally given parameters (Sect. 6.1), so that Drucker–Prager’s parameters can be computed as

$$\begin{aligned} \beta &= \frac{1}{\sqrt{3}} \left(\frac{\sigma_c - \sigma_t}{\sigma_t + \sigma_c} \right) \\ k &= \frac{2}{\sqrt{3}} \left(\frac{\sigma_t \sigma_c}{\sigma_t + \sigma_c} \right). \end{aligned} \quad (62)$$

Given $E = 80 \text{ GPa}$, $\nu = 0.15$, $\sigma_t = 10 \text{ MPa}$ and $l_c = 0.005$, the calibration yields $\alpha_d = 10^{-4}$, $\beta = 0.47$ and $k = 10.50 \text{ MPa}$.

7 Quantification of fracture volume and treatment of the fluid mass balance

The hydraulic fracturing process can either be driven by applying the fluid pressure in the crack directly which can result in unstable crack propagation, or prescribing a constant volume flux. In the latter case, the fluid pressure represents an additional unknown. In order to solve for p or p_f in the system the updated cracked volume V_{crack} , the mass balance $V_{\text{inj}} = V_{\text{crack}}$ is enforced as a constraint where V_{inj} is the injected fluid volume.

While the crack volume is explicitly given in the cohesive zone approach by the displacement jump (cf. Algorithm 1), it is provided by $V_{\text{crack}} = \int_{\Omega} \mathbf{u} \cdot \nabla d \, d\Omega$ in the phase-field model from Γ -convergence considerations. This integral can readily be evaluated by standard finite element routines in the phase-field implementation. In the non-local model, d is not a nodal degree of freedom but a state variable given at integration points. Hence, the gradient of damage is not readily available in a finite element setting and would require additional extra- and interpolation procedures which may induce numerical inaccuracies (Kuhn et al. 2015). Hence, the divergence theorem is applied with the additional assumption of undamaged domain boundaries⁴ to yield $V_{\text{crack}} = \int_{\Omega} d \, (\text{div } \mathbf{u}) \, d\Omega$, which is the formulation used subsequently.

⁴ This assumption is chosen here for simplicity as it is valid in all subsequent test cases. In the more general case, boundary integrals need to be evaluated.

The schemes to update the pressure during the global Newton iterations differ slightly in each implementation. Since both LIE and the non-local model solve only for \mathbf{u} as a primary variable, its update of p is simply done proportional to the volume defect as in Algorithm 1 (LIE) and Algorithm 2 (non-local damage).

Algorithm 1 Incorporation of the volume constraint in the cohesive-zone model.

```

1: while  $V < V_{\text{final}}$  do
2:   update the injected volume,  $V_{\text{inj}}(t_n + \Delta t)$ 
3:   while  $\|p - p_n\|/p \geq \theta_p$  and “no global equilibrium” do
4:     calculate crack volume,  $V_{\text{crack}} = \int_{\Gamma_c} \llbracket \mathbf{u} \rrbracket \cdot \mathbf{n} \, d\Gamma$ 
5:     update pressure  $p = (V_{\text{inj}}/V_{\text{crack}})p_n$ 
6:     update total stress,  $\mathbf{t}_c = \mathbf{t}'_c - dp\mathbf{n}_\Gamma$ 
7:     solve Eq. (3.3) for  $\mathbf{u}$  and  $\mathbf{a}$ 

```

In LIE (Algorithm 1), the primary variables \mathbf{u} and \mathbf{a} are computed with absolute convergence tolerances of 10^{-8} m and 10^{-4} m for the associated residuals $\|\mathbf{R}_u\|$ and $\|\mathbf{R}_a\|$, respectively, the fluid pressure p being with a relative tolerance of $\theta_p = 10^{-4}$.

Algorithm 2 Incorporation of the volume constraint in the non-local plastic-damage model.

```

1: while  $V < V_{\text{final}}$  do
2:   update the injected volume,  $V_{\text{inj}}(t_n + \Delta t)$ 
3:   while  $\|p_{\text{old}} - p\|/p < \theta_p$  and “no global equilibrium” do
4:     calculate crack volume,  $V_{\text{crack}} = \int_{\Omega} d(\text{div } \mathbf{u}) \, d\Omega$ 
5:     update pressure,  $\Delta p = p - p_n = (V_{\text{crack}} - V_{\text{inj}})K_w$ 
6:     update total stress,  $\boldsymbol{\sigma} = \boldsymbol{\sigma}' - dp\mathbf{I}$ 
7:     solve for  $\mathbf{u}$ 

```

In the non-local plastic-damage model (Algorithm 2), the primary variable \mathbf{u} is with an absolute convergence tolerance of $\|\Delta \mathbf{u}\| < 10^{-6}$ m, the fluid pressure's relative tolerance is $\theta_p = 10^{-4}$ and the local stress return algorithm is computed with a relative tolerance of 10^{-10} for the norm of the residuals $\|\mathbf{R}\|$.

Algorithm 3 Incorporation of the volume constraint in the phase-field model.

```

1: while  $V < V_{\text{final}}$  do
2:   update the injected volume,  $V_{\text{inj}}(t_n + \Delta t)$ 
3:   while  $\|d - d_n\| < 10^{-4}$  do
4:     set  $p = 1.0$ 
5:     solve for  $\mathbf{u}_1$ 
6:     calculate crack volume,  $V_1 = \int_{\Omega} \tilde{\mathbf{u}}_1 \cdot \nabla d \, d\Omega$ 
7:     calculate pressure,  $p = V_{\text{inj}}/V_1$ 
8:     update displacement,  $\mathbf{u} = p\mathbf{u}_1$ 
9:     solve for  $d$ 

```

The phase-field implementation solves for both \mathbf{u} and d at the nodes of the finite element discretization. Its update of p is performed at the intermittent stage and addi-

tionally exploits the linearity of the deformation (Algorithm 3). Let \mathbf{u}_1 denote the displacement field under an applied unit pressure $p_1 = 1$: then, due to linearity, the fracture volume is given as $V_{\text{crack}} = p \int_{\Omega} \tilde{\mathbf{u}}_1 \cdot \nabla d \, d\Omega$ which can be inverted to obtain p as in Algorithm 3.

8 Numerical examples of fluid injection into a single fault

In the following, two examples will be considered. The first example addresses a static crack under sub-critical pressurization. The pressure is applied directly such that no fluid mass balance needs to be solved. The example tests the ability of all models to reproduce the pressure-dependent fracture opening profile compared to an analytical solution obtained by elasticity theory.

In the second example, water at room temperature is injected into the crack until it propagates to a certain length. The injection rate of $1 \times 10^{-6} \text{ m}^3 \text{ s}^{-1}$ is chosen so that the corresponding dimensionless viscosity falls in the toughness dominated regime (Garagash 2006; Detournay 2016) where the pressure diffusions are negligible. The injection volume is prescribed as a function of time, requiring the solution of the mass balance. This comparative study thus entails the fracture volume computation, the capturing of the onset of propagation as well as the energy dissipation during propagation.

8.1 Internally pressurised static crack

A widely used classical validation example of an internally pressurised line crack in a two-dimensional plain-strain infinite domain (Ji et al. 2009; Bourdin et al. 2012; Wheeler et al. 2014; Santillán et al. 2017) is considered as a first verification example. The evaluation of the static fracture analysis focuses on the fracture width computation by smeared and discrete approaches. A single crack of length a_0 along the x axis is pressurised by the internal pressure of p in a homogeneous isotropic linear elastic material with the Young's modulus E and Poisson's ratio ν (Fig. 4). Setting $E' = E/(1 - \nu^2)$, the crack opening displacement for $-a_0 \leq x \leq a_0$ (see Sneddon and Lowengrub (1969, Sect. 2.4), for instance) is given by

$$u_y^+(x, 0) = \frac{2pa_0}{E'} \left(1 - \frac{x^2}{a_0^2}\right)^{1/2} = -u_y^-(x, 0). \quad (63)$$

The representation of the initial crack varies between the different approaches.

In the LIE approach, the crack is discretized by one-dimensional quadratic finite elements having a uniform length of 0.01 m. Note, that the entire crack path is predetermined by defining the interface along which the crack will propagate. An initial crack is set by assigning an initial condition to the internal damage variable, $d = 1.0$, at the integration points of the elements in the cracked domain. Irreversibility is accounted for via Eq. (12).

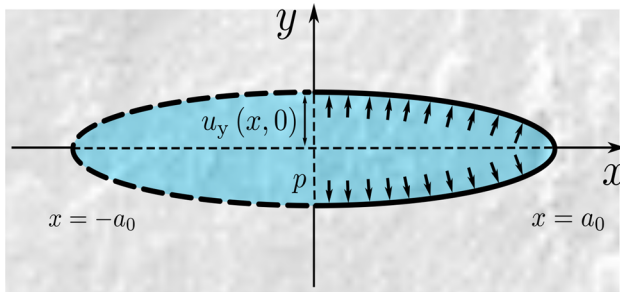


Fig. 4 Internally pressurised crack in 2D infinite domain

In the phase-field approach, the initial crack is represented by specifying $d = 1.0$ at the nodes of the cracked domain and the effective crack length discussed in the previous section is used to evaluate the computational results.

Concerning the damage model, the crack is represented by a damaged area in which $d = 1.0$ is set at the integration points. Because no regularisation is needed for this case (no damage propagation) and to avoid damage diffusion by integral averaging, we have set $l_c = 0$ (equivalent to a local model).

For $a_0 = 0.1$ m and $p = 10$ MPa, computational results from all three methods are compared against the closed form solution in Fig. 5a and their relative errors are shown in Fig. 5b. The errors from the LIE and the phase-field approaches become worse towards the crack tip while those of the non-local plastic-damage model are almost steady along the crack. The LIE and the phase-field may benefit from higher mesh resolution around the tip though, all three models are in good agreement with the closed form solution. Given the static damage profile or the explicit crack, this is essentially an elastic deformation problem and the computational cost is trivial in all three methods. A quadrilateral structured mesh with 0.01 m resolution is used for all the computations. The crack opening profile is explicitly obtained from the displacement jump \mathbf{a} in the LIE approach whereas it is a post-processed quantity in the smeared approaches. It is obtained from a line integral of $\mathbf{u} \cdot \nabla d$ in the phase-field modelling and as the differential nodal displacement of the damaged element for the damage model. Although their matches degrade slightly near the tip, all three methods are capable of computing crack opening displacement quite accurately. Damage performs the worst, as with a single damaged element row, strong gradients are present and not captured as well as in the phase-field case. The LIE approach benefits from the direct incorporation of the strong discontinuity across the crack faces into the formulation, and lies in between the two smeared approaches in the present case.

8.2 Internally pressurised propagating crack

The second verification example addresses the propagation of a fracture by hydraulic forces (Dean and Schmidt 2009; Bourdin et al. 2012; Gupta and Duarte 2014; Lee et al. 2016). Since the work done by the internal pressure is $W = pu_y^+(0, 0)a_0\pi$, the strain energy ($= -\frac{1}{2}W$) is

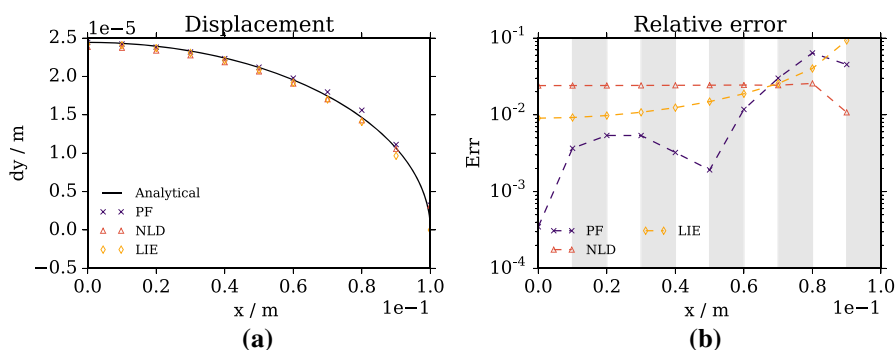


Fig. 5 Comparison of the numerical solution given by the phase-field, non-local damage and LIE methods against the analytical solution **(a)** and relative error of the numerical methods against the analytical solution **(b)**. The transparent bands in **b** indicate the size of the finite element discretization for the phase-field and non-local damage model, which has an influence in the computed displacement field

$$E_b = -\frac{\pi a_0^2 p^2}{E'}. \quad (64)$$

Given material properties (E' and G_c) and the initial fracture geometry (a_0), the critical propagation pressure p_c can be obtained from Griffith's criterion ($-\partial E_b / \partial (2a_0) = G_c$). Hence, fracture propagation occurs when

$$\frac{\pi a_0 p_c^2}{E'} = G_c. \quad (65)$$

Thus the critical pressure can be obtained as⁵

$$p_c = \left[\frac{E' G_c}{\pi a_0} \right]^{1/2}, \quad (66)$$

Also the critical volume is given by

$$V_c = \left[\frac{4\pi a_0^3 G_c}{E'} \right]^{1/2}. \quad (67)$$

Once the pressure reaches p_c (or, equivalently, the volume V_c), the fracture propagates quasi-statically given a prescribed injection volume. As the propagation pressure decreases with the fracture length following Eq. (66), the fracture length a is determined from the internal fracture pressure p as

$$a = \frac{E' G_c}{\pi p^2}, \quad (68)$$

⁵ In terms of the stress intensity factor, $K_{IC} = (E' G_c)^{1/2}$, it is given as $p_c = K_{IC} / \sqrt{\pi a_0}$.

Using the volume, the pressure response can be written as a function of injection volume during fracture propagation as

$$p(V) = \left[\frac{2E'G_c^2}{\pi V} \right]^{1/3}. \quad (69)$$

and the propagating fracture length can also be expressed as a function of injection volume;

$$a(V) = \left[\frac{E'V^2}{4\pi G_c} \right]^{1/3} \quad (70)$$

Comparisons against the closed form solution from all three approaches are shown in Fig. 6. The pressure is slightly overestimated at the peak by the phase-field modelling and converges to the solution as the crack grows (Fig. 6a). Though both fracture toughness and initial crack length are corrected using the approximated effective values [see Eqs. (54) or (56)], the surface energy term may still be slightly overestimated but in an acceptable range ($\sim 2\%$). As the crack length increases and becomes dominant over the internal length, ℓ , the computed pressure converges to the theoretical value. The peak pressure match also improves with finer mesh (i.e. smaller internal length at constant h/ℓ) while accurate crack length evolution prediction can be achieved already with a coarser mesh. This relative insensitivity of crack growth to the internal length (mesh size) agrees with the observations made by Klinsmann et al. (2015) and Zhang et al. (2017). Damage initiation is immediate with the *AT2* model while *AT1* exhibits an elastic regime until failure. With the fine mesh used in this example, both models show an almost identical behaviour. In the computation shown in Fig. 6a, an element edge length of 0.00125 m was used for the linear triangular elements.

The non-local damage model was run with a structured mesh made of linear quadrilateral elements of size 0.00125 m. The solution also satisfactorily reproduces the analytical solution as shown in Fig. 6b, with a higher discrepancy observed in the elastic range compared to the other methods. This is related to the fact that strong gradients across a single element (initial condition) are not captured well by the formulation, as was shown in the static crack case. On the other hand, the model performs best in the inelastic dissipation range during crack propagation phase. The initial crack length is slightly over-estimated because of damage diffusion originating from the non-local averaging formulation and during propagation the over-estimated length is around $\sim 5\%$, which is still an acceptable value. The discrepancy could also be related to the way in which crack-length is computed, i.e., as an integral of damage along a line passing through the center of the damaged zone and parallel to the crack advancing direction. As such, the distribution of damage at the tip decreases from 1 to 0 over a length of roughly ~ 8 elements, i.e., 0.01 m (process length). Applying this correction, the predicted crack length results in a better fit with the analytical solution (black diamonds in Fig. 6b). This discrepancy highlights a long debated concept of smeared approaches to simulate crack problems: where is the exact position of the crack boundary? Being smeared, it is implicit that the crack boundary cannot be precisely assessed, as it is instead a “transition” between intact and fully broken material.

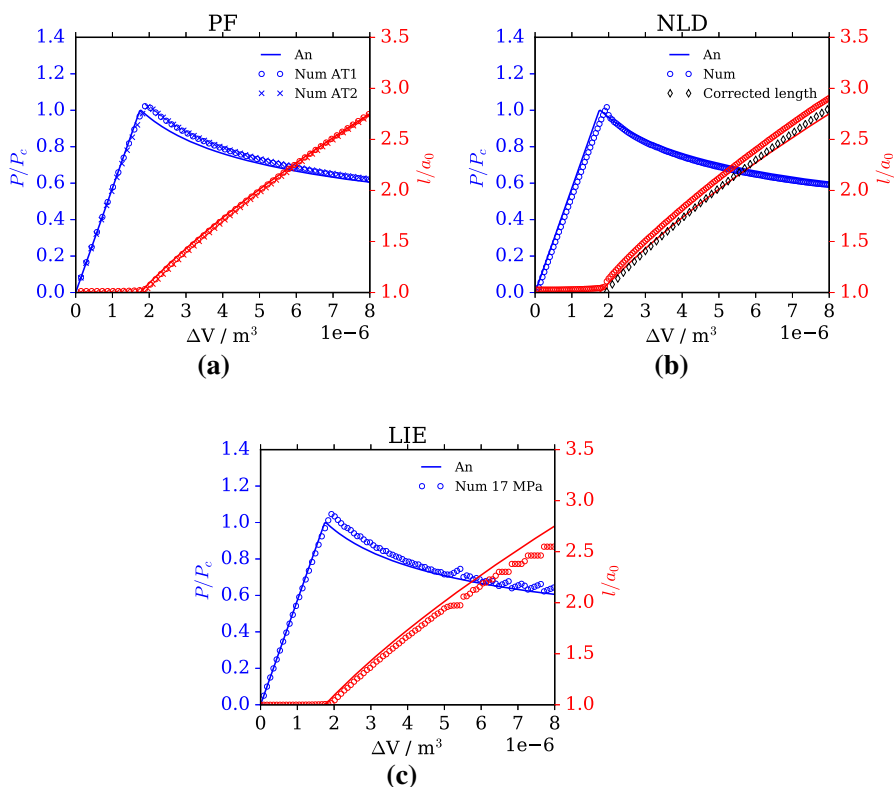


Fig. 6 Analytical and numerical solutions comparison in terms of pressure and crack-length versus injected fluid volume for the phase-field (a), the non-local damage (b) and the lower-dimensional interface element method (c)

In this sense, phase-field methods offer an appealing means to analytically derive an expression for the effective crack length, Eqs. (54) and (56).

Following the guidelines for spatial discretization with respect to the cohesive zone process length ($l_{cz} = 0.00554 \text{ m}$ in case of tensile strength $t_{n,p} = 17 \text{ MPa}$, see Sect. 6.2), a uniform mesh size of 0.00167 m was arranged along the predefined propagation path ahead of the initial crack tip for 0.1 m . After this point, element spacing becomes progressively coarsened with a minimum length of 0.005 m . Once the propagating crack exits the uniformly refined domain, the expected presence of oscillations can be observed in the pressure and crack-length curves (see Fig. 6c). In general, the LIE implementation captures the elastic range very well and shows a slight overestimation of the peak pressure. The solution approaches the analytical curve as the crack propagates.

Figure 7 compares stress profiles at different locations from the three different models. All models reproduce the traction boundary condition on the crack faces, Fig. 7a. Similarly, no appreciable solid stress transfer can be observed for any of the methods across the crack which is a prerequisite for a meaningful stress-field (and displacement) computation. Furthermore, the crack-tip singularity known from linear

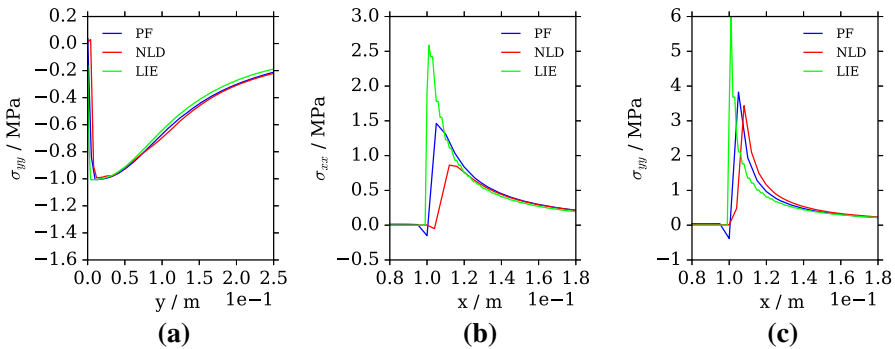


Fig. 7 Stress profiles for the three models: σ_{yy} along a central vertical line (a), σ_{xx} along a central horizontal line (b), σ_{yy} along a central horizontal line (c)

elasticity theory and typically characterised by stress-intensity factors is captured to a varying degree by the different approaches. The high consistency in the stress profile along the central vertical line cross-verifies the successful implementation of the three numerical approaches for the simulation of hydraulic fracturing (see Fig. 7a), while the apparent discrepancies in the stress peak values and peak position (see Fig. 7b, c) show that the LIE approach is most consistent with linear elastic fracture mechanics in terms of stress profiles under the present conditions.

Unlike the other two methods, stresses are not explicitly defined in the phase-field model and the mechanical variables (e.g. displacement and stress) do not have clear physical meanings in the phase transition zone (near the crack) even though its jump set can be quantified from an integral. In the non-local plastic-damage model, the crack propagates when the available strength is mobilised. Due to the mode I loading, the stress state at the tip is tension dominated such that tensile strength becomes the relevant quantity.

Although this study does not particularly aim to compare the computational efficiencies, a few observations made through this limited set of examples indicate that both the phase-field and non-local damage models are much more computationally efficient than the lower-interface element model and that the mesh sensitivity of the lower-interface element model is greater than those of the phase-field model and the non-local damage. In order for the lower-interface element method to achieve similar accuracy to the other two approaches, it required a finer mesh size and significantly greater number of iterations, both of which contribute to its computational time. Apart from this general remark, however, we will restrict ourselves from further commenting on the computational efficiencies as computation time does not depend only on the method but also on the implementation, and its comparison would require more carefully devised measures, which is beyond the scope of the current study.

9 Conclusion

We have presented three different numerical methodologies to simulate hydraulic fracturing. The cohesive zone model based on locally enriched interface elements treats cracks discretely along element edges. Crack propagation is thus discretization-dependent and, for practical purposes, requires a priori knowledge about the crack propagation path. A mesh-independent generalization of the present approach would lead to well-known extended finite element methods associated with drastically increased implementational effort.

Since cracks are represented implicitly in both phase-field and non-local damage models using a dedicated damage variable, neither special element formulations nor prescribed crack paths are required. In the phase-field model, the damage variable is a solution obtained through successive energy minimisation consistent with linear elastic fracture mechanics whereas it is an internal variable, non-locally averaged over a region of influence, in the non-local damage model.

The cohesive model approximates fracture mechanics using a traction-separation law, which requires two additional parameters (e.g. the stiffness, the cohesive strength, or the critical separation displacement) aside from the fracture toughness. The variational phase-field formulation is originally derived from Griffith's fracture mechanics introducing one additional parameter, the internal length, in its regularised phase-field form. It is shown, however, that the computational result is relatively insensitive to the internal length in a toughness-dominated (or non strength-dominated), i.e. fracture mechanical, regime unless the defect (crack) size is comparable to the internal length. The non-local damage model needs a full definition of the yield surface and flow rule for plasticity and some more additional parameters to describe damage evolution. As such, it can well describe strength evolution at different confinements, dilatancy, rate of softening and mixed-mode fracture propagation (not discussed here). Its extension to ductile fracture may proceed without major model changes, a benefit which has not been exploited in the present study. On the other hand, it is very difficult to relate material parameters to fracture energy, which does not enter the formulation explicitly as strains in the dissipation zone are almost never known a-priori. Though this subject has been addressed in literature before (Jirásek 1998; Nguyen and Houlsby 2007; Nguyen et al. 2015), we feel the question remains open as any calibration will necessarily depend on structural size and remain problem-specific. Capitalizing on the advantage of its versatility, one suggestion is to follow alternative paths in the parameter calibration process (e.g., representing full stress strain response in triaxial strength and fracture mechanics tests, cf. Parisio et al. 2018a). In Sect. 6, we have discussed how each of the models can be set up to simulate a brittle fracture behaviour.

From our comparative analyses, it has been evidenced that all three approaches can successfully represent hydraulic fracture propagation in a toughness-dominated regime. The cohesive zone model has the strong advantage of directly accounting for enhanced displacement field in its formulation, which is not the case for the smeared approaches. In the phase-field model, discrete variables such as crack volume or crack aperture opening can be readily approximated from the gradient of the damage field using the Γ -convergence property. The non-local formulation requires the analyst to make an appropriate choice. Concerning propagation, it is clear that both phase-field

and non-local damage are better suited to represent crack propagation when the crack path is not known in advance such as in case of complex stress fields, mixed-mode and rotating crack propagation. In such cases, the LIE implementation would require special treatments such as crack tracking and h-adaptive remeshing algorithms. The implementation effort would be significant especially in three-dimensional settings and if branching or merging crack needs to be considered, criteria for all possible variations would be required explicitly.

Our results have shed light on the advantages and drawbacks of some of the most popular numerical techniques employed to simulate hydraulic-fracture propagation. Furthermore, based on each underlying theoretical model we have shown how to obtain key process quantities as well as how to consistently parametrize each of the methods. While the presented examples are all two dimensional, the implementation of all methods in OpenGeoSys is done for three dimensional problems as well. This is connected to additional coding for the LIE implementation but none at all for the smeared approaches.

The discussions in this paper are limited to hydraulic fracturing scenarios where the assumption of a toughness-dominated regime is valid, i.e. for the cases viscous dissipation and leak-off are irrelevant. Comparing the numerical approaches with respect to their conceptual ease as well as numerical accuracy and efficiency in other settings is the subject of ongoing studies.

Acknowledgements We thank Dr.-Ing. Thomas Frühwirth and Prof. Dr.-Ing. habil. Heinz Konietzky from the Institute of Geotechnics, Chair of Rock Mechanics at the TU Bergakademie Freiberg for providing us with the material properties of the local gneiss. The authors gratefully acknowledge the funding provided by the German Federal Ministry of Education and Research (BMBF) for the GeoInt project, Grant Number 03G0866A, as well as the support of the Project Management Jülich (PtJ). The contribution of F.P. was financed by the GEMex project. The GEMex project is supported by the European Union's Horizon 2020 programme for Research and Innovation under Grant Agreement No 727550.

Appendix

A Rescaling of the phase-field energy functional (non-dimensionalization)

The scaling of Eq. (23) to achieve a non-dimensional format proceeds as follows. Let ψ_0 , x_0 , u_0 , and $\tau_0 = p_0$ be scaling factors, and

$$\psi = \psi_0 \tilde{\psi} \quad (71)$$

$$\mathbf{x} = x_0 \tilde{\mathbf{x}} \quad (72)$$

$$\mathbf{u} = u_0 \tilde{\mathbf{u}} \quad (73)$$

$$p = p_0 \tilde{p} \quad (74)$$

$$\tilde{\mathbf{t}} = \tau_0 \tilde{\mathbf{t}} \quad \text{and} \quad \varrho \mathbf{b} = \tau_0 \varrho \tilde{\mathbf{b}} \quad (75)$$

where $\tilde{\Omega}$ is a dimensionless variable. Thus, Eq. (23) becomes

$$\begin{aligned} E(\mathbf{u}, d, p) = & \psi_0 u_0^2 x_0^{n-2} \int_{\Omega} d^2 \tilde{\psi}^+(\tilde{\mathbf{u}}) + \tilde{\psi}^-(\tilde{\mathbf{u}}) \, d\Omega - \tau_0 x_0^{n-1} u_0 \int_{\partial_N \Omega} \tilde{\mathbf{t}} \cdot \tilde{\mathbf{u}} \, d\Gamma - \\ & - \tau_0 x_0^{n-1} u_0 \int_{\Omega} \tilde{\varrho} \tilde{\mathbf{b}} \cdot \tilde{\mathbf{u}} \, d\Omega + x_0^{n-1} \frac{G_c}{4c_w} \int_{\Omega} \left(\frac{w(d)}{\ell} + \ell |\nabla d|^2 \right) \, d\Omega \\ & + p_0 x_0^{n-1} u_0 \int_{\Omega} \tilde{p} \tilde{\mathbf{u}} \cdot \nabla d \, d\Omega \end{aligned} \quad (76)$$

Dividing both sides by $\psi_0 u_0^2 x_0^{n-2}$,

$$\begin{aligned} \tilde{E}(\tilde{\mathbf{u}}, d, \tilde{p}) = & \int_{\Omega} d^2 \tilde{\psi}^+(\tilde{\mathbf{u}}) + \tilde{\psi}^-(\tilde{\mathbf{u}}) \, d\Omega - \frac{\tau_0 x_0}{u_0 \psi_0} \int_{\partial_N \Omega} \tilde{\mathbf{t}} \cdot \tilde{\mathbf{u}} \, d\Gamma - \\ & - \frac{\tau_0 x_0}{u_0 \psi_0} \int_{\Omega} \tilde{\varrho} \tilde{\mathbf{b}} \cdot \tilde{\mathbf{u}} \, d\Omega + \frac{G_c x_0}{4c_w \psi_0 u_0^2} \int_{\Omega} \left(\frac{w(d)}{\ell} + \ell |\nabla d|^2 \right) \, d\Omega \quad (77) \\ & + \frac{p_0 x_0}{u_0 \psi_0} \int_{\Omega} \tilde{p} \tilde{\mathbf{u}} \cdot \nabla d \, d\Omega \end{aligned}$$

and setting

$$x_0 = \frac{\psi_0 u_0^2}{G_c} \quad (78)$$

$$\tau_0 = p_0 = \frac{\psi_0 u_0}{x_0} \quad (79)$$

yields the numerically favourable formulation

$$\begin{aligned} \tilde{E}(\tilde{\mathbf{u}}, d, \tilde{p}) = & \int_{\Omega} d^2 \tilde{\psi}^+(\tilde{\mathbf{u}}) + \tilde{\psi}^-(\tilde{\mathbf{u}}) \, d\Omega - \int_{\partial_N \Omega} \tilde{\mathbf{t}} \cdot \tilde{\mathbf{u}} \, d\Gamma - \\ & - \int_{\Omega} \tilde{\mathbf{t}} \cdot \tilde{\mathbf{u}} \, d\Omega + \frac{1}{4c_w} \int_{\Omega} \left(\frac{w(d)}{\ell} + \ell |\nabla d|^2 \right) \, d\Omega + \int_{\Omega} \tilde{p} \tilde{\mathbf{u}} \cdot \nabla d \, d\Omega \end{aligned} \quad (80)$$

References

- Alessi, R., Marigo, J.J., Vidoli, S.: Gradient damage models coupled with plasticity: variational formulation and main properties. *Mech. Mater.* **80**(PB), 351–367 (2015). <https://doi.org/10.1016/j.mechmat.2013.12.005>
- Ambati, M., Gerasimov, T., De Lorenzis, L.: Phase-field modeling of ductile fracture. *Comput. Mech.* **55**(5), 1017–1040 (2015). <https://doi.org/10.1007/s00466-015-1151-4>. arXiv:1011.1669v3
- Ambrosio, L., Tortorelli, V.M.: Approximation of functional depending on jumps by elliptic functional via t-convergence. *Commun. Pure Appl. Math.* **43**(8), 999–1036 (1990). <https://doi.org/10.1002/cpa.3160430805>
- Ambrosio, L., Tortorelli, V.M.: On the approximation of free discontinuity problems. *Boll. Unione Mat. Ital.* **7**, 105–123 (1992)

- Amor, H., Marigo, J.J., Maurini, C.: Regularized formulation of the variational brittle fracture with unilateral contact: Numerical experiments. *J. Mech. Phys. Solids* **57**(8), 1209–1229 (2009). <https://doi.org/10.1016/j.jmps.2009.04.011>
- Balay, S., Gropp, W.D., McInnes, L.C., Smith, B.F.: Efficient management of parallelism in object oriented numerical software libraries. In: Arge, E., Bruaset, A.M., Langtangen, H.P. (eds.) *Modern Software Tools in Scientific Computing*, pp. 163–202. Birkhäuser Press, Basel (1997)
- Balay, S., Abhyankar, S., Adams, M.F., Brown, J., Brune, P., Buschelman, K., Dalcin, L., Eijkhout, V., Gropp, W.D., Kaushik, D., Knepley, M.G., May, D.A., McInnes, L.C., Rupp, K., Sanan, P., Smith, B.F., Zampini, S., Zhang, H., Zhang, H.: PETSc users manual. Technical Report ANL-95/11—Revision 3.8, Argonne National Laboratory (2017a). <http://www.mcs.anl.gov/petsc>
- Balay, S., Abhyankar, S., Adams, M.F., Brown, J., Brune, P., Buschelman, K., Dalcin, L., Eijkhout, V., Gropp, W.D., Kaushik, D., Knepley, M.G., May, D.A., McInnes, L.C., Rupp, K., Smith, B.F., Zampini, S., Zhang, H., Zhang, H.: PETSc Web page (2017b). <http://www.mcs.anl.gov/petsc>, <http://www.mcs.anl.gov/petsc>
- Bazant, P.Z., Jirasek, M.: Nonlocal integral formulations of plasticity and damage: survey of progress. *J. Eng. Mech.* **128**, 1119–1149 (2002)
- Bažant, Z.P.: Why continuum damage is nonlocal: micromechanics arguments. *J. Eng. Mech.* **117**(5), 1070–1087 (1991)
- Belytschko, T., Moës, N., Usui, S., Parimi, C.: Arbitrary discontinuities in finite elements. *Int. J. Numer. Methods Eng.* **50**(4), 993–1013 (2001)
- Belytschko, T., Chen, H., Xu, J., Zi, G.: Dynamic crack propagation based on loss of hyperbolicity and a new discontinuous enrichment. *Int. J. Numer. Methods Eng.* **58**(12), 1873–1905 (2003)
- Belytschko, T., Gracie, R., Ventura, G.: A review of extended/generalized finite element methods for material modeling. *Model. Simul. Mater. Sci. Eng.* **17**(4), 043001 (2009)
- Biot, M.: General theory of three-dimensional consolidation. *J. Appl. Phys.* **12**(2), 155–164 (1941)
- Böger, L., Keip, M.A., Miehe, C.: Minimization and saddle-point principles for the phase-field modeling of fracture in hydrogels. *Comput. Mater. Sci.* **138**, 474–485 (2017)
- Borden, M.J., Verhoosel, C.V., Scott, M.A., Hughes, T.J., Landis, C.M.: A phase-field description of dynamic brittle fracture. *Comput. Methods Appl. Mech. Eng.* **217–220**, 77–95 (2012). <https://doi.org/10.1016/j.cma.2012.01.008>
- Bouchard, P.O., Bay, F., Chastel, Y., Tovina, I.: Crack propagation modelling using an advanced remeshing technique. *Comput. Methods Appl. Mech. Eng.* **189**(3), 723–742 (2000)
- Bourdin, B., Francfort, G., Marigo, J.J.: Numerical experiments in revisited brittle fracture. *J. Mech. Phys. Solids* **48**(4), 797–826 (2000). [https://doi.org/10.1016/S0022-5096\(99\)00028-9](https://doi.org/10.1016/S0022-5096(99)00028-9)
- Bourdin, B., Francfort, G.A., Marigo, J.J.: The variational approach to fracture. *J. Elast.* **91**, 5–148 (2008)
- Bourdin, B., Chukwudozie, C., Yoshioka, K.: A variational approach to the numerical simulation of hydraulic fracturing. In: *Proceedings of the 2012 SPE Annual Technical Conference and Exhibition*, vol. SPE 159154 (2012)
- Bourdin, B., Marigo, J.J., Maurini, C., Sicsic, P.: Morphogenesis and propagation of complex cracks induced by thermal shocks. *Phys. Rev. Lett.* **112**, 014301 (2014). <https://doi.org/10.1103/PhysRevLett.112.014301>
- Brace, W., Paulding, B., Scholz, C.: Dilatancy in the fracture of crystalline rocks. *J. Geophys. Res.* **71**(16), 3939–3953 (1966)
- Braides, A.: *Approximation of Free-Discontinuity Problems*. Springer, Berlin (1998)
- Branco, R., Antunes, F., Costa, J.: A review on 3D-FE adaptive remeshing techniques for crack growth modelling. *Eng. Fract. Mech.* **141**, 170–195 (2015)
- Budyn, E., Zi, G., Moës, N., Belytschko, T.: A method for multiple crack growth in brittle materials without remeshing. *Int. J. Numer. Methods Eng.* **61**(10), 1741–1770 (2004)
- Chessa, J., Belytschko, T.: An extended finite element method for two-phase fluids. *J. Appl. Mech.* **70**(1), 10–17 (2003)
- Chukwudozie, C.: *Application of the variational fracture model to hydraulic fracturing in poroelastic media*. Dissertation, Louisiana State University (2016)
- Davila, C., Camanho, P., de Moura, M.: Mixed-mode decohesion elements for analyses of progressive delamination. In: *19th AIAA Applied Aerodynamics Conference*, p. 1486 (2001)
- de Borst, R., Verhoosel, C.V.: Gradient damage vs phase-field approaches for fracture: similarities and differences. *Comput. Methods Appl. Mech. Eng.* **312**, 78–94 (2016a)

- de Borst, R., Verhoosel, C.V.: Gradient damage vs phase-field approaches for fracture: similarities and differences. *Comput. Methods Appl. Mech. Eng.* **312**, 78–94 (2016b)
- Dean, R.H., Schmidt, J.H.: Hydraulic-fracture predictions with a fully coupled geomechanical reservoir simulator. *SPEJ* (2009). <https://doi.org/10.2118/116470-PA>
- Desmorat, R., Gatuíngt, F., Jirásek, M.: Nonlocal models with damage-dependent interactions motivated by internal time. *Eng. Fract. Mech.* **142**, 255–275 (2015)
- Detournay, E.: Mechanics of hydraulic fractures. *Annu. Rev. Fluid Mech.* **48**, 311–339 (2016)
- Diederichs, M.: Manuel rocha medal recipient rock fracture and collapse under low confinement conditions. *Rock Mech. Rock Eng.* **36**(5), 339–381 (2003)
- Duarte, C.A., Reno, L., Simone, A.: A high-order generalized fem for through-the-thickness branched cracks. *Int. J. Numer. Methods Eng.* **72**(3), 325–351 (2007)
- Duddu, R., Waisman, H.: A nonlocal continuum damage mechanics approach to simulation of creep fracture in ice sheets. *Comput. Mech.* **51**(6), 961–974 (2013)
- Economides, M.J., Nolte, E.K.G.: *Reservoir Stimulation*, vol. 2. Wiley, New York (2000)
- Elices, M., Guinea, G., Gomez, J., Planas, J.: The cohesive zone model: advantages, limitations and challenges. *Eng. Fract. Mech.* **69**(2), 137–163 (2002)
- Francfort, G., Marigo, J.J.: Revisiting brittle fracture as an energy minimization problem. *J. Mech. Phys. Solids* **46**(8), 1319–1342 (1998). [https://doi.org/10.1016/S0022-5096\(98\)00034-9](https://doi.org/10.1016/S0022-5096(98)00034-9)
- Freddi, F., Royer-Carfagni, G.: Regularized variational theories of fracture: a unified approach. *J. Mech. Phys. Solids* (2010). <https://doi.org/10.1016/j.jmps.2010.02.010>
- Fries, T.P., Belytschko, T.: The intrinsic XFEM: a method for arbitrary discontinuities without additional unknowns. *Int. J. Numer. Methods Eng.* **68**(13), 1358–1385 (2006)
- Fries, T.P., Schätzer, M., Weber, N.: XFEM-simulation of hydraulic fracturing in 3D with emphasis on stress intensity factors. In: Oñate, E., Oliver, J., Huerta, A. (eds.) 11th World Congress on Computational Mechanics (WCCM XI), 5th European Conference on Computational Mechanics (ECCM V), 6th European Conference on Computational Fluid Dynamics (ECFD VI) (2014)
- Garagash, D.I.: Plane-strain propagation of a fluid-driven fracture during injection and shut-in: asymptotics of large toughness. *Eng. Fract. Mech.* **73**(4), 456–481 (2006). <https://doi.org/10.1016/j.engfracmech.2005.07.012>
- Gasser, T.C., Holzapfel, G.A.: Modeling 3D crack propagation in unreinforced concrete using PUFEM. *Comput. Methods Appl. Mech. Eng.* **194**(25–26), 2859–2896 (2005)
- Giovanardi, B., Scotti, A., Formaggia, L.: A hybrid XFEM-phase field (xfield) method for crack propagation in brittle elastic materials. *Comput. Methods Appl. Mech. Eng.* **320**, 396–420 (2017)
- Gordeliy, E., Peirce, A.: Coupling schemes for modeling hydraulic fracture propagation using the XFEM. *Comput. Methods Appl. Mech. Eng.* **253**, 305–322 (2013)
- Gupta, P., Duarte, C.A.: Particle shape effect on macro-and micro behaviours of monodisperse ellipsoids. *Int. J. Numer. Anal. Methods Geomech.* **38**, 1397–1430 (2014). <https://doi.org/10.1002/nag.732>
- He, W., Wu, Y.F., Xu, Y., Fu, T.T.: A thermodynamically consistent nonlocal damage model for concrete materials with unilateral effects. *Comput. Methods Appl. Mech. Eng.* **297**, 371–391 (2015)
- Heider, Y., Markert, B.: Simulation of hydraulic fracture of porous materials using the phase-field modeling approach. *Pamm* **16**(1), 447–448 (2016). <https://doi.org/10.1002/pamm.201610212>
- Hillerborg, A., Modéer, M., Petersson, P.E.: Analysis of crack formation and crack growth in concrete by means of fracture mechanics and finite elements. *Cement Concr. Res.* **6**(6), 773–781 (1976)
- Hoek, E., Martin, C.: Fracture initiation and propagation in intact rock—a review. *J. Rock Mech. Geotech. Eng.* **6**(4), 287–300 (2014)
- Ji, J., Settari, A., Sullivan, R.: A novel hydraulic fracturing model fully coupled with geomechanics and reservoir simulation. *SPE J.* (2009). <https://doi.org/10.2118/110845-PA>
- Jiang, L., Sainoki, A., Mitri, H.S., Ma, N., Liu, H., Hao, Z.: Influence of fracture-induced weakening on coal mine gateroad stability. *Int. J. Rock Mech. Min. Sci.* **88**, 307–317 (2016). <https://doi.org/10.1016/j.ijrmms.2016.04.017>
- Jirásek, M.: Comparison of nonlocal models for damage and fracture. LSC Report 98(02) (1998)
- Johnson, L., Marschall, P., Zuidema, P., Gribo, P.: Effects of post-disposal gas generation in a repository for spent fuel, high-level waste and long-lived intermediate level waste sited in opalinus clay. Technical Report, National Cooperative for the Disposal of Radioactive Waste (NAGRA) (2004)
- Karma, A., Kessler, D.A., Levine, H.: Phase-field model of mode III dynamic fracture. *Phys. Rev. Lett.* **87**(4), 3–6 (2001). <https://doi.org/10.1103/PhysRevLett.87.045501>
- Khoei, A.R.: *Extended Finite Element Method: Theory and Applications*. Wiley, London (2014)

- Khoei, A., Moslemi, H., Sharifi, M.: Three-dimensional cohesive fracture modeling of non-planar crack growth using adaptive FE technique. *Int. J. Solids Struct.* **49**(17), 2334–2348 (2012)
- Klinsmann, M., Rosato, D., Kamlah, M., McMeeking, R.M.: An assessment of the phase field formulation for crack growth. *Comput. Methods Appl. Mech. Eng.* **294**(Supplement C), 313–330 (2015). <https://doi.org/10.1016/j.cma.2015.06.009>
- Kolditz, O., Bauer, S., Bilke, L., Böttcher, N., Delfs, J., Fischer, T., Görke, U., Kalbacher, T., Kosakowski, G., McDermott, C., et al.: OpenGeoSys: an open-source initiative for numerical simulation of thermo-hydro-mechanical/chemical (THM/C) processes in porous media. *Environ. Earth Sci.* **67**(2), 589–599 (2012)
- Kuhl, E., Ramm, E., de Borst, R.: An anisotropic gradient damage model for quasi-brittle materials. *Comput. Methods Appl. Mech. Eng.* **183**(1), 87–103 (2000)
- Kuhn, C., Müller, R.: A continuum phase field model for fracture. *Eng. Fract. Mech.* **77**(18), 3625–3634 (2010). <https://doi.org/10.1016/j.engfracmech.2010.08.009>. (**computational Mechanics in Fracture and Damage: A Special Issue in Honor of Prof. Gross**)
- Kuhn, C., Lohkamp, R., Schneider, F., Aurich, J.C., Mueller, R.: Finite element computation of discrete configurational forces in crystal plasticity. *Int. J. Solids Struct.* **56**, 62–77 (2015)
- Lee, S., Wheeler, M.F., Wick, T.: Pressure and fluid-driven fracture propagation in porous media using an adaptive finite element phase field model. *Comput. Methods Appl. Mech. Eng.* **312**, 509–541 (2016). <https://doi.org/10.1016/j.cma.2016.02.037>
- Legarth, B., Huenges, E., Zimmermann, G.: Hydraulic fracturing in a sedimentary geothermal reservoir: results and implications. *Int. J. Rock Mech. Min. Sci.* **42**(7–8), 1028–1041 (2005)
- Lemaitre, J., Chaboche, J.L., Benallal, A., Desmorat, R.: *Mécanique des matériaux solides-3eme édition*. Dunod (2009)
- Li, T., Marigo, J.J., Guilbaud, D., Potapov, S.: Gradient damage modeling of brittle fracture in an explicit dynamic context. *Int. J. Numer. Methods Eng.* **00**(March), 1–25 (2016). <https://doi.org/10.1002/nme>
- Marigo, J.J., Maurini, C., Pham, K.: An overview of the modelling of fracture by gradient damage models. *Meccanica* **51**(12), 3107–3128 (2016). <https://doi.org/10.1007/s11012-016-0538-4>
- Meschke, G., Leonhart, D.: A generalized finite element method for hydro-mechanically coupled analysis of hydraulic fracturing problems using space–time variant enrichment functions. *Comput. Methods Appl. Mech. Eng.* **290**, 438–465 (2015)
- Meschke, G., Dumstorff, P., Fleming, W.: Variational extended finite element model for cohesive cracks: influence of integration and interface law. In: *IUTAM Symposium on Discretization Methods for Evolving Discontinuities*, pp. 283–301. Springer (2007)
- Meyer, A., Rabold, F., Scherzer, M.: Efficient finite element simulation of crack propagation. *Preprintreihe des Chemnitz SFB 393* (2004)
- Miehe, C., Welschinger, F., Hofacker, M.: Thermodynamically consistent phase-field models of fracture: variational principles and multi-field fe implementations. *Int. J. Numer. Methods Eng.* **83**(10), 1273–1311 (2010). <https://doi.org/10.1002/nme.2861>
- Miehe, C., Mauthe, S., Teichtmeister, S.: *Minimization Principles for the Coupled Problem of Darcy–Biot-Type Fluid Transport in Porous Media Linked to Phase Field Modeling of Fracture*, vol. 82. Elsevier, Amsterdam (2015). <https://doi.org/10.1016/j.jmps.2015.04.006>
- Miehe, C., Aldakheel, F., Raina, A.: *Phase Field Modeling of Ductile Fracture at Finite Strains: A Variational Gradient-extended Plasticity-damage Theory*, vol. 84. Elsevier, Amsterdam (2016). <https://doi.org/10.1016/j.ijplas.2016.04.011>
- Minkley, W., Brückner, D., Lüdeling, C.: Tightness of salt rocks and fluid percolation. In: *45. Geomechanik-Kolloquium, Freiberg, Germany* (2016)
- Moës, N., Belytschko, T.: Extended finite element method for cohesive crack growth. *Eng. Fract. Mech.* **69**(7), 813–833 (2002)
- Moës, N., Dolbow, J., Belytschko, T.: A finite element method for crack growth without remeshing. *Int. J. Numer. Methods Eng.* **46**(1), 131–150 (1999)
- Morita, N., Black, A.D., Guh, G.F.: *Theory of Lost Circulation Pressure*. SPE Annual Technical Conference and Exhibition, 23–26 September, New Orleans, Louisiana (1990). <https://doi.org/10.2118/20409-MS>
- Murakami, S.: *Continuum Damage Mechanics: A Continuum Mechanics Approach to the Analysis of Damage and Fracture*, vol. 185. Springer, Berlin (2012)
- Nagel, T., Görke, U.J., Moerman, K.M., Kolditz, O.: On advantages of the kelvin mapping in finite element implementations of deformation processes. *Environ. Earth Sci.* **75**(11), 1–11 (2016). <https://doi.org/10.1007/s12665-016-5429-4>

- Nagel, T., Minkley, W., Böttcher, N., Naumov, D., Görke, U.J., Kolditz, O.: Implicit numerical integration and consistent linearization of inelastic constitutive models of rock salt. *Comput. Struct.* **182**, 87–103 (2017)
- Nedjar, B.: On a concept of directional damage gradient in transversely isotropic materials. *Int. J. Solids Struct.* **88**, 56–67 (2016)
- Needleman, A.: An analysis of decohesion along an imperfect interface. *Int. J. Fract.* **42**(1), 21–40 (1990a)
- Needleman, A.: An analysis of tensile decohesion along an interface. *J. Mech. Phys. Solids* **38**(3), 289–324 (1990b)
- Nguyen, G.D., Houlsby, G.T.: Non-local damage modelling of concrete: a procedure for the determination of model parameters. *Int. J. Numer. Anal. Methods Geomech.* **31**(7), 867–891 (2007)
- Nguyen, O., Repetto, E., Ortiz, M., Radovitzky, R.: A cohesive model of fatigue crack growth. *Int. J. Fract.* **110**(4), 351–369 (2001)
- Nguyen, G.D., Korsunsky, A.M., Belnoue, J.P.H.: A nonlocal coupled damage-plasticity model for the analysis of ductile failure. *Int. J. Plast.* **64**, 56–75 (2015)
- Oliver, J.: On the discrete constitutive models induced by strong discontinuity kinematics and continuum constitutive equations. *Int. J. Solids Struct.* **37**(48–50), 7207–7229 (2000)
- Oliver, J., Huespe, A.E., Pulido, M., Chaves, E.: From continuum mechanics to fracture mechanics: the strong discontinuity approach. *Eng. Fract. Mech.* **69**(2), 113–136 (2002)
- Pariso, F., Laloui, L.: Plastic-damage modeling of saturated quasi-brittle shales. *Int. J. Rock Mech. Min. Sci.* **93**, 295–306 (2017)
- Pariso, F., Samat, S., Laloui, L.: Constitutive analysis of shale: a coupled damage plasticity approach. *Int. J. Solids Struct.* **75**, 88–98 (2015)
- Pariso, F., Tarokh, A., Makhnenko, R., Naumov, D., Miao, X.Y., Kolditz, O., Nagel, T.: Experimental characterization and numerical modelling of fracture processes in granite. *Int. J. Solids Struct.* (2018a, in press). <https://doi.org/10.1016/j.ijsolstr.2018.12.019>
- Pariso, F., Vilarasa, V., Laloui, L.: Hydro-mechanical modeling of tunnel excavation in anisotropic shale with coupled damage-plasticity and micro-dilatant regularization. *Rock Mech. Rock Eng.* (2018b) <https://doi.org/10.1007/s00603-018-1569-z>
- Peerlings, R.H.J., De Borst, R., Brekelmans, W.A.M., De Vree, J.H.P.: Gradient enhanced damage for quasi-brittle materials. *Int. J. Numer. Methods Eng.* **39**(19), 3391–3403 (1996)
- Pham, K., Amor, H., Marigo, J.J., Maurini, C.: Gradient damage models and their use to approximate brittle fracture. *Int. J. Damage Mech.* **20**(4), 618–652 (2011). <https://doi.org/10.1177/1056789510386852>
- Rice, J.: *The Mechanics of Earthquake Rupture*. Division of Engineering, Brown University, Providence (1979)
- Roth, S.N., Léger, P., Soulaïmani, A.: Coupled hydro-mechanical cracking of concrete using XFEM in 3D. In: Saouma, V., Bolander, J., Landis, E. (eds.) 9th International Conference on Fracture Mechanics of Concrete and Concrete Structures FraMCoS-9 (2016)
- Santillán, D., Juanes, R., Cueto-Felgueroso, L.: Phase field model of fluid-driven fracture in elastic media: immersed-fracture formulation and validation with analytical solutions. *J. Geophys. Res. Solid Earth* **122**(4), 2565–2589 (2017). <https://doi.org/10.1002/2016JB013572>
- Silani, M., Talebi, H., Hamouda, A.M., Rabczuk, T.: Nonlocal damage modelling in clay/epoxy nanocomposites using a multiscale approach. *J. Comput. Sci.* **15**, 18–23 (2016)
- Sneddon, I., Lowengrub, M.: *Crack Problems in the Classical Theory of Elasticity*. The SIAM Series in Applied Mathematics. Wiley, London (1969)
- Tanné, E., Li, T., Bourdin, B., Marigo, J.J., Maurini, C.: Crack nucleation in variational phase-field models of brittle fracture. *J. Mech. Phys. Solids* **110**(Supplement C), 80–99 (2018). <https://doi.org/10.1016/j.jmps.2017.09.006>
- Turon, A., Davila, C.G., Camanho, P.P., Costa, J.: An engineering solution for mesh size effects in the simulation of delamination using cohesive zone models. *Eng. Fract. Mech.* **74**(10), 1665–1682 (2007)
- Vtorushin, E.: Application of mixed finite elements to spatially non-local model of inelastic deformations. *GEM-Int. J. Geomath.* **7**(2), 183–201 (2016)
- Watanabe, N., Wang, W., Taron, J., Görke, U., Kolditz, O.: Lower-dimensional interface elements with local enrichment: application to coupled hydro-mechanical problems in discretely fractured porous media. *Int. J. Numer. Methods Eng.* **90**(8), 1010–1034 (2012). <https://doi.org/10.1002/nme.3353/full>
- Wheeler, M., Wick, T., Wollner, W.: An augmented-lagrangian method for the phase-field approach for pressurized fractures. *Comput. Methods Appl. Mech. Eng.* **271**(Supplement C), 69–85 (2014). <https://doi.org/10.1016/j.cma.2013.12.005>

- Wilson, Z.A., Landis, C.M.: Phase-field modeling of hydraulic fracture. *J. Mech. Phys. Solids* **96**, 264–290 (2016). <https://doi.org/10.1016/j.jmps.2016.07.019>
- Yoshioka, K., Bourdin, B.: A variational hydraulic fracturing model coupled to a reservoir simulator. *Int. J. Rock Mech. Min. Sci.* **88**(Supplement C), 137–150 (2016). <https://doi.org/10.1016/j.ijrmms.2016.07.020>
- Zhang, Z., Guazzato, M., Sornsuwan, T., Scherrer, S.S., Rungsiyakull, C., Li, W., Swain, M.V., Li, Q.: Thermally induced fracture for core-veneered dental ceramic structures. *Acta Biomater.* **9**(9), 8394–8402 (2013)
- Zhang, X., Vignes, C., Sloan, S.W., Sheng, D.: Numerical evaluation of the phase-field model for brittle fracture with emphasis on the length scale. *Comput. Mech.* **59**(5), 737–752 (2017). <https://doi.org/10.1007/s00466-017-1373-8>

Publisher's Note Springer Nature remains neutral with regard to jurisdictional claims in published maps and institutional affiliations.

Affiliations

Keita Yoshioka¹ · Francesco Parisio¹ · Dmitri Naumov¹ · Renchao Lu^{1,2} ·
Olaf Kolditz^{1,2} · Thomas Nagel^{1,3} 

Keita Yoshioka
keita.yoshioka@ufz.de

- ¹ Department of Environmental Informatics, Helmholtz Centre for Environmental Research – UFZ, Leipzig, Germany
- ² Applied Environmental Systems Analysis, Technische Universität Dresden, Dresden, Germany
- ³ Chair of Soil Mechanics and Foundation Engineering, Geotechnical Institute, Technische Universität Bergakademie Freiberg, Freiberg, Germany